

Showcasing research from Prof. Yuichi Negishi's laboratory, Tohoku University, Japan.

Metal-organic frameworks as promising electrocatalysts for the nitrogen reduction reaction: mapping the research landscape and identifying future trends

This review provides a comprehensive overview of metal-organic frameworks (MOFs) catalyst design protocols from molecular building blocks to extended networks and how precisely designed MOF electrocatalyst structures can explicitly control targeted NRR reaction pathways, besides giving an insight into the future scopes and challenges.

As featured in:



See Saikat Das, Yuichi Negishi *et al.*, *J. Mater. Chem. A*, 2024, **12**, 26350.

Cite this: *J. Mater. Chem. A*, 2024, 12, 26350

# Metal–organic frameworks as promising electrocatalysts for the nitrogen reduction reaction: mapping the research landscape and identifying future trends

Riki Nakatani, <sup>a</sup> Saikat Das \*<sup>a</sup> and Yuichi Negishi \*<sup>ab</sup>

Since the pioneering discovery of metal–organic frameworks (MOFs) a quarter century ago, they have evolved as a new category of porous crystalline extended network structures with atomic/molecular level designability. The distinctive porosity and structural customizability of MOFs have been crucial to their wide spectrum of applications. Among these applications, MOFs have gained prominence as electrocatalysts in the nitrogen reduction reaction (NRR), which has inimitable potential to solve environmental crises. The reticular structures of MOFs with uniformly distributed active sites and their easy accessibility endow them with enhanced catalytic activity. In this review, we provide a comprehensive overview of MOF catalyst design protocols from molecular building blocks to extended networks, and discuss how precisely designed MOF electrocatalyst structures can explicitly control targeted NRR pathways, besides giving an insight into the future prospects and challenges.

Received 11th July 2024  
Accepted 4th September 2024

DOI: 10.1039/d4ta04817b

rsc.li/materials-a

## 1. Introduction

Since the seminal discovery of metal–organic frameworks (MOFs) as cutting-edge porous inorganic–organic hybrid materials following zeolites, they have come a long way in terms of fundamental studies and practical applications.<sup>1,2</sup> MOFs are assembled materials that consist of metal ions or nanoclusters as nodes (nodes are also regarded as secondary building units,

SBUs) and electron-donating organic molecules as multidentate linkers that are linked through coordination bonds.<sup>3–6</sup> The combination of a wide range of metals and linkers results in a variety of physicochemical properties: pore metrics and environment, internal surface area, optoelectronic characteristics and so forth. Furthermore, the structures have superb stability and crystallinity coupled with high porosity. Therefore, a plethora of applications (gas separation, drug delivery, water harvesting, biomedicine, sensing, magnetism, proton conduction, *etc.*) have been explored to leverage the intrinsic advantages of MOFs.<sup>7–13</sup> MOFs have captivated the scientific community and hitherto approximately 100 000 MOFs have

<sup>a</sup>Department of Applied Chemistry, Faculty of Science, Tokyo University of Science, 1-3 Kagurazaka, Shinjuku-ku, Tokyo 162-8601, Japan. E-mail: saikatdas@rs.tus.ac.jp

<sup>b</sup>Institute of Multidisciplinary Research for Advanced Materials, Tohoku University, 2-1-1 Katahira, Aoba-ku, Sendai 980-8577, Japan. E-mail: yuichi.negishi.a8@tohoku.ac.jp



Riki Nakatani

Riki Nakatani is a first year Master's course student in Prof. Negishi's group at Tokyo University of Science (TUS). His research interests include the synthesis of metal–organic frameworks (MOFs) for energy and environmental applications.



Saikat Das

Saikat Das is a Junior Associate Professor in Prof. Negishi's group at TUS. He received his PhD degree in Chemistry and Physics of Polymers (2018) from Jilin University, China, under the supervision of Prof. Teng Ben. His research interests encompass the designed construction of novel MOFs and covalent organic frameworks (COFs).



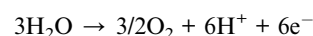
been reported.<sup>14</sup> As of now, the momentum for research in this field remains strong.

Studies in recent years have documented a diverse range of materials harnessed for heterogeneous catalysis research that include supported metal nanoparticles,<sup>15</sup> nanoclusters,<sup>16</sup> single atoms,<sup>17</sup> metal oxides,<sup>18</sup> zeolites,<sup>19</sup> mesoporous silica,<sup>20</sup> MOFs,<sup>21</sup> and covalent organic frameworks (COFs),<sup>22</sup> among others. Progress notwithstanding, significant gaps still exist, which necessitates addressing several limitations and challenges: (i) the activity, selectivity and durability of functional heterogeneous catalysts for targeted reactions fall well short due to structural degradation and challenges of achieving precise conditions and intricate techniques for the controlled synthesis of catalysts; (ii) the structural and chemical complexity of heterogeneous catalyst systems leads to a poor comprehension of the mechanisms of surface-catalysed reactions and structure–activity correlations, which hinders systematic design approaches to optimal catalysts.<sup>23</sup> Regarding the development and optimization of heterogeneous catalysts, we should maintain a proper balance between material-specific properties and properties that are defined by the relationship of the catalyst with its environment. Accordingly, the materials suitable as heterogeneous catalysts must be endowed with the following characteristics: first, the design and synthesis of materials should be in favor of achieving a uniform and dispersed active site distribution; the former ensures high selectivity toward the products of interest while the latter results in high activity. Second, the structure of catalytic materials needs to be sufficiently robust so as to achieve high activity while allowing long-term stability and recyclability over consecutive runs. Third, the tailorability of the material components could provide precise control over catalytic activity and selectivity at the atomic level.

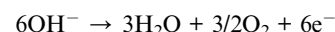
Ammonia (NH<sub>3</sub>) is necessary to produce nitrogen-based fertilizers and is extensively used as a carbon-free energy source, serving as an alternative to fossil fuels.<sup>24</sup> On the other hand, nitrogen occupying the majority of the atmosphere possesses high stability and chemical inactivity because of its triple bond. In early 20th century, Fitz Haber and Carl Bosch developed the breakthrough process, known as Haber–Bosch

process, which produced NH<sub>3</sub> from N<sub>2</sub> and H<sub>2</sub> with a single pass conversion of usually 10–15%.<sup>25,26</sup> However, the reaction is energy-intensive and entails catalysts operating at elevated temperatures of 400–550 °C and pressures of 15–25 MPa.<sup>27</sup> As a result, 2% of energy consumption and 0.5% of green-house gas emission in the world are attributed to this process.<sup>28</sup> Therefore, the eco-friendly nitrogen reduction reaction (NRR) utilizing low energy is highly coveted. The electrocatalytic NRR is attracting the attention of the scientific community as a clean and green sustainable approach.<sup>29</sup> The electrochemical NRR (eNRR) is capable of producing NH<sub>3</sub> from N<sub>2</sub> gas and H<sub>2</sub>O as a hydrogen source at ambient temperature and pressure, consuming much lower energy than conventional processes.<sup>30</sup> Herein, we show the reactions occurring at each electrode as follows:<sup>31</sup>

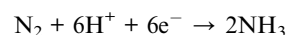
Anode reaction (in acid electrolyte):



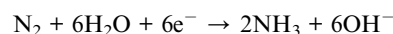
Anode reaction (in base electrolyte):



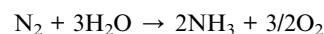
Cathode reaction (in acid electrolyte):



Cathode reaction (in base electrolyte):



Overall reaction:



As the eNRR is an emerging field with increasing research interest, numerous materials have been tested as catalysts for the eNRR. Transition metals such as Ru, Mo, Rh and Fe have been actively studied for improving NRR activity by facilitating the cleavage of N≡N bonds.<sup>32</sup> Transition metal oxides are enticing catalysts for enhancing NRR activity by forming oxygen vacancies and doping heteroatoms or metals, which function as reaction sites.<sup>33</sup> However, transition metal oxides face challenges such as low electrical conductivity, poor stability under acidic conditions, and weak adsorption strength, which limit their activity in the NRR.<sup>34</sup> Single-atom catalysts (SACs) minimize the amount of metal and allow each individual metal atom to drive the reaction. Nevertheless, they are known to face stability issues, as single atoms tend to aggregate during the eNRR. To overcome this issue, aggregation while maintaining sufficient active sites should be prevented, although this approach is still under investigation.<sup>35</sup> In addition to the aforementioned metal catalysts, environment-friendly catalysts



Yuichi Negishi

*Yuichi Negishi is currently a Professor at the Institute of Multidisciplinary Research for Advanced Materials at Tohoku University. He received his PhD degree in Chemistry (2001) from Keio University under the supervision of Prof. Atsushi Nakajima. He was employed as an Assistant Professor at Keio University and the Institute for Molecular Science. Prior to joining Tohoku University, he was a Professor at TUS. His research interests*

*include the structural and functional exploration of atomically precise metal nanoclusters, MOFs and COFs.*



that do not use metals, such as graphene,  $g\text{-C}_3\text{N}_4$ , COFs, *etc.* have also been developed.<sup>36</sup> These non-metal electrocatalysts are suitable for the NRR because their low proton adsorption ability suppresses the HER. However, they exhibit a low nitrogen conversion rate and low current density in  $\text{NH}_3$  production, resulting in lower  $\text{NH}_3$  generation efficiency compared to metal catalysts, which makes their practical application difficult. As hybrid materials composed of metal atoms and organic ligands, MOFs provide some remarkable merits as catalysts for the eNRR: (i) MOFs enable atomically precise structural design; (ii) MOFs have the potential to function as molecular sieves, which increases the concentration of specific molecules; and (iii) the ordered lattice structure provides well-defined active sites, which simplifies the consideration of reaction mechanisms.

Regarding the catalysts used for the eNRR, their stability and conductivity are not yet up to the mark and pose challenges.<sup>37</sup> Commonly, most MOFs behave as insulators (conductivity  $<10^{-10}$  S  $\text{cm}^{-1}$ ) owing to the absence of energy pathway for charge transport or free charge carriers.<sup>38</sup> However, recently some methods have successfully provided MOFs with sufficient conductivity, enabling their utilization in electrochemical applications: implementing specific linkers, introducing guest molecules, and loading with conducting hosts, among others.<sup>39</sup> Additionally, the kind of metals used to construct MOFs is also one of the important factors to consider in catalysis, which decides the cost and versatility. Since the first research on MOFs exploited as eNRR catalysts, subsequent studies have enriched this field substantially. Notably, some previous reviews have already provided an overview of MOFs as catalysts for the NRR.<sup>40–45</sup> However, there is still a need for in-depth investigation of the correlation between catalytic activities and atomic-level structures of MOFs, as well as recent experimental and theoretical developments in this field. This review provides a unique perspective on understanding the NRR mechanisms and strategies by exploring the interplay of metal sites, functional modules, catalytic species, defects and the confined microenvironment in the MOF crystalline structure. In this review, we illustrate the core concepts of the NRR, avant-garde MOFs harnessed for the NRR, design processes and recent developments in MOF electrocatalysts, as well as chronologically trace the journey of NRR electrocatalysts with MOFs. In terms of unique traits of MOFs, they have ordered uniformity and porosity that enable guest molecules to access active sites readily. Furthermore, we discuss future directions to advance this field in the last section of this review.

## 2. The history of pristine MOFs as electrocatalysts

MOFs are highly designable porous materials that can be constructed by changing the combinations of diverse linkers and metal nodes. Hence, MOFs enable precise designability well-suited for specific applications by adjusting the precursors.<sup>46</sup> In this section, we will introduce the evolution of MOFs utilized

as electrocatalysts by presenting notable research across various electrochemical reactions.

### 2.1. MOFs as electrocatalysts for the HER

The electrocatalytic hydrogen evolution reaction (HER) from water is considered as a promising route for producing hydrogen, which can be utilized as a sustainable energy carrier thereby addressing energy and environmental concerns. In 2011, non-noble metal polyoxometalate-based MOF  $\epsilon(\text{trim})_{4/3}$ ,  $(\text{TBA})_3 \cdot [\text{PMo}^{\text{V}}_8\text{Mo}^{\text{VI}}_4\text{O}_{36}(\text{OH})_4\text{Zn}_4][\text{C}_6\text{H}_3(\text{COO})_3]_{4/3} \cdot 6\text{H}_2\text{O}$ , was employed as the HER catalyst by Dolbecq and co-workers.<sup>47</sup> To perform this reaction, a carbon paste modified electrode for introducing POMOF (POMOF/CPE) was applied. The cyclic voltammetry (CV) results displayed a peak that was associated with the HER process. The HER turnover frequency of  $\epsilon(\text{trim})_{4/3}$ /CPE was *ca.* 6.7  $\text{s}^{-1}$  with a 200 mV overpotential in water. Encouraged by the potential of cobalt dithiolene as a catalyst for the HER from water,<sup>48</sup> the Marinescu group integrated it into two-dimensional (2D) Co MOFs (MOS1 and MOS2) to study its competency for the same application.<sup>49</sup> The faradaic yield of  $\text{H}_2$  was  $97 \pm 3\%$  with MOS1 on a glassy carbon (GC) electrode at pH = 2.6 and  $-0.8$  V *vs.* the standard hydrogen electrode (SHE). A research study by the Li group in 2021 showed that  $\text{NiRu}_x\text{-BDC}$  served as the electrocatalyst for the HER.<sup>50</sup> As revealed by linear sweep voltammetry (LSV) measurements,  $\text{NiRu}_{0.13}\text{-BDC}$  exhibited the highest HER activity (the overpotential to reach 10  $\text{mA cm}^{-2}$  was 36 mV) among various  $\text{NiRu}_x\text{-BDC}$  MOFs with different molar ratios of Ru/Ni and Ni-BDC in phosphate buffered saline solution. The Tafel slopes also indicated that  $\text{NiRu}_{0.13}\text{-BDC}$  possessed the most promising potential to implement it for the HER. Furthermore, the electrocatalytic activity of  $\text{NiRu}_{0.13}\text{-BDC}$  was also confirmed in acidic and basic solutions (1 M HCl and KOH aqueous), where it still showcased good HER activities.

### 2.2. MOFs as electrocatalysts for the OER

Constructing highly efficient and selective electrocatalysts is critical to convert water into value-added chemicals like oxygen *via* the oxygen evolution reaction (OER) in order to achieve sustainability in efficient energy utilization. By virtue of their distinct structural features, MOFs have gained recognition as OER electrocatalysts, displaying noteworthy activity, selectivity and stability. In 2010, a study by Marken and colleagues showed that the Fe(BTC) MOF was used as an electrocatalyst for the OER.<sup>51</sup> This reaction was conducted in NaOH containing 0.1 M KCl solution as the electrolyte. The peak current was found to be in direct proportion with hydroxide concentration. The number of electrons releasing from each hydroxide was calculated to be 0.63, which plausibly explains the generation of oxygen. In 2016, Liu, Zhao, and Tang *et al.* investigated the electrocatalytic OER activity of NiCo-UMOFNs.<sup>52</sup> The onset potential and overpotential of NiCo-UMOFNs on GC were 1.42 V *vs.* RHE and 1.479 V *vs.* RHE at 10  $\text{mA cm}^{-2}$ , respectively, and both values were lower than those of Ni-UMOFNs, Co-UMOFNs and bulk NiCo-MOFs. Moreover, changing CP to conductive copper foam enhanced OER activity, which was revealed by the shifts of onset



potential and overpotential. The FE of NiCo-UMOFNs reached 99.3% and no appreciable changes in anodic current could be observed for 200 hours at an overpotential of 0.25 V, demonstrating greater stability than RuO<sub>2</sub>. In 2019, Liu, Li and co-workers prepared CoBDC and then introduced Fc as a missing linker instead of BDC, thereby resulting in CoBDC-Fc<sub>x</sub>, where *x* represents the molar ratio of Fc/Fc + BDC.<sup>53</sup> These MOFs were deposited on nickel foam (NF) and utilized as self-supported electrodes (CoBDC-NF and CoBDC-Fc<sub>x</sub>-NF). The overpotential to reach 10 mA cm<sup>-2</sup> and Tafel slope for CoBDC-NF were 252 mV and 63 mV dec<sup>-1</sup>, respectively, and the corresponding values for CoBDC-Fc<sub>x</sub>-NF were 178 mV and 51 mV dec<sup>-1</sup>, respectively. Additionally, the stability of CoBDC-Fc<sub>x</sub>-NF was assessed by chronopotentiometry test and CV, which disclosed greater stability of CoBDC-Fc<sub>x</sub>-NF.

### 2.3. MOFs as electrocatalysts for the ORR

The oxygen reduction reaction (ORR) is an electrochemical reaction of pivotal importance in energy conversion and storage systems like fuel cells. In 2012, Mao *et al.*, for the first time, used MOFs as ORR electrocatalysts.<sup>54</sup> Two novel copper-based MOFs, Cu-BTC and Cu-bipy-BTC were employed. GC electrodes were coated with MOFs (hereinafter Cu-BTC-modified GC and Cu-bipy-modified GC) and the electrocatalysis performance was confirmed by CV. Cu-BTC-modified GC showed superior performance in the ORR to only GC. However, the Cu-BTC-modified GC electrode was unstable under aqueous conditions. On the other hand, Cu-bipy-BTC-modified GC showed enough stability under the same conditions. Moreover, Cu-bipy-BTC-modified GC showed commendable electrocatalytic activity toward nearly 4e-reduction of O<sub>2</sub>, as evidenced by CV measurements. In 2016, a conductive 2D MOF, Ni<sub>3</sub>(HITP)<sub>2</sub>, was employed by Dincă and co-workers as an electrocatalyst for the ORR.<sup>55</sup> The ORR onset potential was 0.82 V *vs.* RHE in 0.1 M KOH with a current density of -50 μA cm<sup>-2</sup>, which implied the highest ORR activities among non-platinum group metal catalysts. The stability of Ni<sub>3</sub>(HITP)<sub>2</sub> was demonstrated through steady-state potentiostatic measurements with a potential of 0.77 V and the results revealed that the current density remained practically the same for more than 8 hours with a marginal decrease. A study by Cao and colleagues made use of zeolitic imidazolate frameworks (ZIFs) as the support for integrating Co porphyrins on the surface by ligand exchange upon the synthesis of ZIFs.<sup>56</sup> The ORR Tafel plot of Co tetra(imidazolyl) porphyrin onto ZIF-8 (1@ZIF-8) showcased a slope of 53 mV dec<sup>-1</sup>, which was more gradual than the values of the compound precursors (1 : 62 mV dec<sup>-1</sup>, ZIF-8: 82 mV dec<sup>-1</sup>) and Pt/C (66 mV dec<sup>-1</sup>). The product selectivity of 1@ZIF-8 was confirmed by calculating the number (*n*) of electrons transferred per O<sub>2</sub> and the value was 2.65, which implied lower selectivity than 1 (2.82), ZIF-8 (2.73) and Pt/C (3.92). Furthermore, to increase the selectivity of H<sub>2</sub>O production, ZIF-67 was introduced (1@ZIF-67) and this compound enabled to ameliorate the selectivity (*n* = 3.70). Another Co porphyrin ligand, Co tetra(4-imidazolylphenyl) porphyrin (hereinafter 2), was utilized instead of 1, and the *n* value of 2@ZIF-8 was 2.70 while that of

2@ZIF-67 was 3.70, which suggested the importance of distances between the Co ion into the porphyrin macrocycle and the MOF surface for better selectivity.

### 2.4. MOFs as electrocatalysts for the CRR

The overuse of fossil fuels has resulted in a drastic increase in CO<sub>2</sub> concentration in air and is one of the root causes of global warming. Over the past few years, many research endeavors have engaged in utilizing CO<sub>2</sub> to tackle the environmental concerns and energy scarcity. In 2012, Hinogami *et al.* implemented a new protocol to adopt MOFs as electrocatalysts for the CO<sub>2</sub> reduction reaction (CRR).<sup>57</sup> The MOF was constructed using Cu ions and rubeanic acid (denoted as CR-MOF), and the MOF slurry was dropped on conductive carbon paper (CP). CR-MOF electrodes generated HCOOH with an efficiency of 30% at -1.2 V, -1.4 V and -1.6 V *vs.* SHE, and the selectivity of HCOOH exceeded 98%. Additionally, the performance of CR-MOF and Cu metal electrodes was compared based on the amount of HCOOH produced (13.4 μmol cm<sup>-2</sup> h<sup>-1</sup> and 1.1 μmol cm<sup>-2</sup> h<sup>-1</sup>, respectively) under the same conditions at -1.2 V *vs.* SHE. In 2016, Zhu, Han and colleagues implemented the Zn-BTC MOF for the electrocatalytic CRR in imidazolium based ionic liquid (IL) electrolytes for the first time.<sup>58</sup> Zn-BTC was deposited on CP by the electrophoretic deposition technique and the resulting composite was named Zn-MOF/CP. The products obtained after the CRR by utilizing Zn-MOF/CP and IL BmimBF<sub>4</sub> were mainly CH<sub>4</sub> with small amounts of CO and H<sub>2</sub> after a 2 hour reaction at -2.2 V *vs.* Ag/AgCl. Furthermore, the electrocatalytic study was scrutinized by comparing with other several ILs: BmimOTf, BmimPF<sub>6</sub> and BmimClO<sub>4</sub>. The results suggested that existing F in ILs played an important role in achieving higher total current density (*j*<sub>tot</sub>) on account of interaction with CO<sub>2</sub>. Compared to other metal cathodes under the same conditions, both *j*<sub>tot</sub> and selectivity of CH<sub>4</sub> of Zn-MOF/CP were remarkably better. In 2018, a research study by Lan and co-workers reported a CP based gas diffusion electrode (GDE) with Cu<sub>3</sub>(BTC)<sub>2</sub> for CO<sub>2</sub> capture (hereinafter GDE-CuMOF-*x*, *x* represents the mass ratio of Cu-MOF, *x* = 5, 7.5, 10, 15, and 20).<sup>59</sup> The reduction currents of the GDE and GDE-CuMOF-*x* were measured, and each of the GDEs modified with CuMOF displayed lower values than the pristine GDE, which suggested the suppression of the HER as evident from the linear sweep voltammogram. The FEs for CH<sub>4</sub> of GDE-CuMOF-5, 7.5, 10, and 15 were more than twice higher than that of the GDE at high overpotentials. Additionally, the best FEs for C<sub>2</sub>H<sub>4</sub> were achieved when GDE-CuMOF-10 was leveraged. Moreover, the FE for H<sub>2</sub> evolution was lowest for GDE-CuMOF-10. Regarding stability, GDE-CuMOF-10 exhibited higher stability at -2.5 V *vs.* the saturated calomel electrode for 6 hours relative to the GDE.

### 2.5. MOFs as electrocatalysts for the EER

In 2010, Kitagawa and colleagues pioneered the use of [(HOC<sub>2</sub>H<sub>4</sub>)<sub>2</sub>dtoaCu] as a nonnoble-MOF catalyst for the ethanol electrooxidation reaction (EER).<sup>60</sup> The conductivity of this MOF reached 3.3 × 10<sup>-4</sup> S cm<sup>-1</sup>. This MOF also showed stability against sulfuric acid (1 M, 80 °C) and elevated temperatures



( $\sim 165$  °C), making it suitable for use as an electrocatalyst. In this work, acetaldehyde, oxidation product of ethanol, was produced with the highest conversion ratio of 6.8% within 20 minutes (ethanol concentration was 0.5 M and the electrolyte volume was 20 mL).

### 3. Background and state of the art of the NRR

#### 3.1. The pathway of the NRR

The mechanism of the NRR encompasses various pathways occurring on the surface of heterogeneous catalysts. In this section, we will explain the NRR mechanisms that have been reported in previous research studies.

In the dissociative pathway, the  $\text{N}\equiv\text{N}$  bond in the  $\text{N}_2$  molecule is first broken and each separated N atom is adsorbed on the surface of the catalyst. Following this, the hydrogenation of N atoms occurs and  $\text{NH}_3$  molecules are generated and released (Fig. 1a). In this process, the first reaction needs high energy because of the strong  $\text{N}\equiv\text{N}$  bond. In practice, the Haber–Bosch process typically follows this pathway.<sup>61</sup>

In the associative alternating pathway, the  $\text{N}_2$  molecule is initially chemisorbed on the active sites in an end-on configuration. Secondly, hydrogenation takes place and one bond of

$\text{N}\equiv\text{N}$  is severed. After that, another hydrogenation reaction occurs and the second bond of  $\text{N}=\text{N}$  is severed. Finally, hydrogenation happens and two  $\text{NH}_3$  molecules are produced in sequence (Fig. 1b).

The associative distal pathway also follows the same procedure as the associative alternating pathway until the halfway point. After being connected with the surface of the catalyst, the preferential hydrogenation of the nitrogen atom that is not adsorbed on the surface and the amputation of the  $\text{N}\equiv\text{N}$  bond gradually occur, and  $\text{NH}_3$  molecules are generated. After this, the nitrogen atom that is adsorbed on the surface also undergoes hydrogenation and a  $\text{NH}_3$  molecule is formed (Fig. 1c).

In the enzymatic pathway, first, a  $\text{N}_2$  molecule is attached in a side-on configuration on the catalyst surface. After this, hydrogenation of both N atoms occurs and one bond of  $\text{N}\equiv\text{N}$  is cleaved. Furthermore, the same process occurs again. Subsequently, a  $\text{NH}_3$  molecule is generated and released. Finally, the remaining N atom is converted to  $\text{NH}_3$  through hydrogenation and released (Fig. 1d).

The MvK pathway unfolds on the surface of TMN catalysts.<sup>62</sup> Initially, the N atom which exists on the surface connects H atoms. After reduction of the N atom, the N atom is released as  $\text{NH}_3$ . Following this, vacancies are created on the surface and

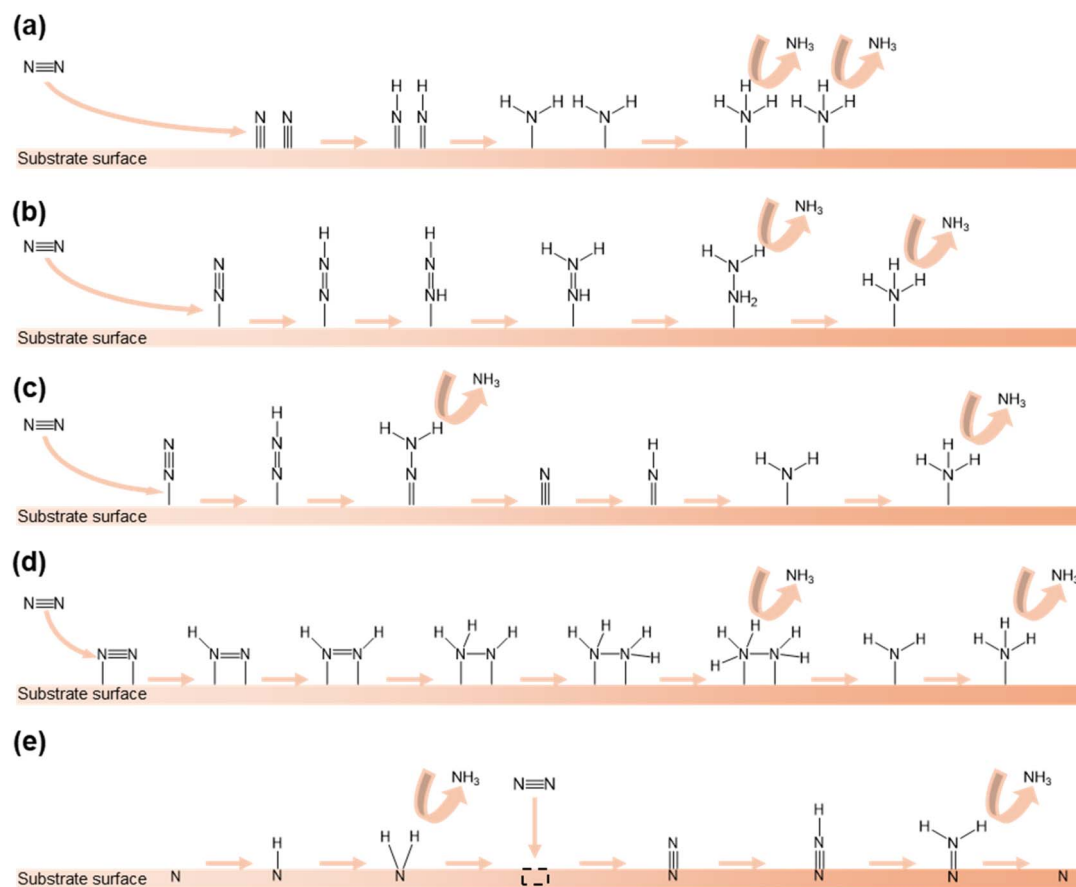


Fig. 1 Different pathways of the NRR: (a) dissociative pathway, (b) associative alternating pathway, (c) associative distal pathway, (d) enzymatic pathway, and (e) MvK pathway.



the incoming  $N_2$  molecule is stuffed into the vacancy. Subsequently, the N atom which is not stuffed undergoes hydrogenation and is released as  $NH_3$ . Finally, the remaining N atom regenerates the surface of the catalyst (Fig. 1e).

### 3.2. Methods for detecting $NH_3$ and $N_2H_4$

One of the crucial factors in evaluating the performance of the NRR is the quantitative evaluation of the generated amount of  $NH_3$  as well as other potential by-products. This evaluation serves as a pivotal metric for comparing different catalysts in terms of efficacy. In this section, we discuss the detection techniques for the product  $NH_3$  and by-product hydrazine ( $N_2H_4$ ), which were utilized in NRR research with MOFs.

**3.2.1. Indophenol method.** The indophenol method based on the Berthelot reaction has been widely utilized for the detection of  $NH_3$  for many years.<sup>63,64</sup> Herein, we will introduce the basic procedure for this detection as reported by Scheiner in 1976.<sup>65</sup> In this method, there are some advantages: (1) Solutions with a pH range from 3 to 11.5 can measure the amount of ammonia nitrogen without the need for any correlation because of the establishment of a buffer system; (2) regarding the limit of detection, the small amount of  $NH_3$  solutions (the concentrations ranging from 0.02 to 1 mg  $L^{-1}$ ) can be detected by this method when 1 cm cells are implemented; (3) the stability of color showed high durability under ambient conditions, which is proved by the reacted solution maintaining its color for at least 48 h. To observe this reaction, some reagents were prepared: (1) buffer solution was synthesized using  $Na_3PO_4 \cdot 12H_2O$ ,  $C_6H_5Na_3O_7 \cdot 2H_2O$  and EDTA which were dissolved in water; (2) phenol nitroprusside solution was made using  $C_6H_5OH$ ,  $Na_2[Fe(CN)_5(NO)] \cdot 2H_2O$  and a buffer solution; (3) alkaline hypochlorite solution was obtained from  $HClO$ , 1 M NaOH aqueous solution and water. The samples, phenol nitroprusside solution and alkaline hypochlorite solution, were mixed until color development was complete. In this reaction, nitroprusside was used as the catalyst for the indophenol formation reaction.<sup>66</sup> After waiting for some time, the UV-vis absorbance spectrum was measured and the peak at 635 nm was utilized for the detection of ammonia nitrogen by using a calibration curve. The advantage of this method is its ease of measurement. However, the color may fade over time, and its stability significantly decreases under highly alkaline conditions. The mechanism suggested by Bolleter and co-workers<sup>63</sup> is represented in Fig. 2.

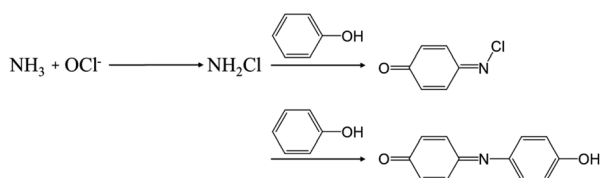


Fig. 2 The overall indophenol method reaction between  $HClO$ , phenol and  $NH_3$  presented by Bolleter and colleagues. Adapted with permission from ref. 63. Copyright 1961, American Chemical Society.

**3.2.2. The colorimetric method using the Nessler reagent.** This method is also used for calculating the amount of ammonia nitrogen by measuring color changes. The Nessler reagent is a solution composed of mercuric iodide, potassium iodide and alkaline reagent (*e.g.*,  $KOH$ ).<sup>67,68</sup> In this reaction, the product was isolated as a yellow-brown precipitate ( $NHg_2I$ ). Subsequently, UV-vis absorbance measurement was conducted.<sup>69</sup> This reaction is called nesslerization.<sup>70</sup> Similar to the indophenol method, this method has the advantage of being easy to conduct and evaluate. Nevertheless, the mercury compound contained in the Nessler reagent is toxic to human health, leading to its declining use in recent research.

**3.2.3. Electrochemical detection.** In this method, an ammonia ion selective electrode was adopted for  $NH_3$  detection. Firstly, a series of standard  $NH_3$  solutions with different concentrations were prepared.<sup>71,72</sup> In the next step, the electrometer calibration was accomplished and the standard curve with the  $Y$  axis and  $X$  axis representing potential and concentration, respectively, was obtained. Finally, the sample was added, and the concentration was confirmed from the electrode slope. This method allows for accurate measurement with minimum time-dependent changes. On the other hand, this method requires more effort and money compared to absorbance measurement.

**3.2.4. NMR detection method with isotopes.** NMR measurement can also detect products of the NRR. NMR with isotope labeling is the most reliable approach for identifying the origin of  $NH_3$  and excluding possible environmental contaminants. Typically, due to the simplicity of quantitative analysis by colorimetry, this method is often utilized as a preparatory tool to check the existence of  $NH_3$ , which is generated from the reaction.

**3.2.5. The Watt and Chrisp method for  $N_2H_4$  detection.** In this subsection, we will explain the method for the detection of by-product  $N_2H_4$ , which has been commonly utilized. This method also utilizes the absorbance at a wavelength of 458 nm, wherein color alteration results from the reaction of *p*-dimethylaminobenzaldehyde with a solution of hydrazine in  $HCl$ .<sup>73</sup> This color revealed no obvious change for at least 12 hours, which indicates the merits of this method in terms of stability. The suitable concentration of  $N_2H_4$  was between 0.06 and 0.47 ppm (the relative error within 1%) and the  $N_2H_4$  concentration up to 0.77 ppm followed the Lambert–Beer law.

## 4. MOFs as electrocatalysts for the NRR

In this section, we will elucidate recent research reports on the utilization of MOFs as electrocatalysts for the NRR.

### 4.1. Single metal MOFs for the NRR

In 2017, Yin and co-workers utilized three MOFs (denoted as MOF (Fe), MOF (Co) and MOF (Cu)) as electrocatalysts for the NRR at low temperature and ambient pressure.<sup>74</sup>  $H_2O$  and  $N_2$  (or air) were used as the precursors for this NRR. Under  $-1.2$  V vs.  $Ag/AgCl$  and 90 °C conditions with water and  $N_2$  gas, the highest



rates of  $\text{NH}_3$  generation in the case of MOF (Fe), MOF (Co) and MOF (Cu) were  $2.12 \times 10^{-9} \text{ mol s}^{-1} \text{ cm}^{-2}$ ,  $1.64 \times 10^{-9} \text{ mol s}^{-1} \text{ cm}^{-2}$  and  $1.24 \times 10^{-9} \text{ mol s}^{-1} \text{ cm}^{-2}$ , respectively. Moreover, they utilized water and air instead of  $\text{N}_2$  as the raw materials and MOF (Fe) as the reaction catalyst under the same conditions. The results implied that the highest  $\text{NH}_3$  production rate was  $1.52 \times 10^{-9} \text{ mol s}^{-1} \text{ cm}^{-2}$ . The highest current efficiencies for MOF (Fe), MOF (Co) and MOF (Cu) utilizing water and  $\text{N}_2$ , and for MOF (Fe) using water and air were 1.43, 1.06, 0.96 and 0.88%, respectively, at 1.2 V vs. Ag/AgCl and 90 °C.

In 2019, Wei and co-workers employed a self-supported catalyst  $\text{Cu}^{\text{II}}$ -MOF,  $[\text{Cu}_{24}\text{L}_{12}(\text{H}_2\text{O})_{12}] \cdot 30\text{DMF} \cdot 14\text{H}_2\text{O}$ , on carbon cloth (represented as JUC-1000/CC) as the cathode and anode for both the NRR and oxidation of SG to GA.<sup>75</sup> First, JUC-1000/CC was utilized as the working electrode in the  $\text{N}_2$ -saturated 1.0 M  $\text{Na}_2\text{SO}_4$  solution electrolyte. As a result, the  $\text{NH}_3$  generation rate and FE were as high as  $13.274 \mu\text{g h}^{-1} \text{ mg}_{\text{cat}}^{-1}$  and 1.519% at  $-0.3 \text{ V vs. RHE}$ , respectively. In addition, this electrode was used as both the cathode and anode for the SG oxidation reaction and NRR in a 1.0 M SG solution. The results evinced that the highest  $\text{NH}_3$  generation rate and FE were  $24.7 \mu\text{g h}^{-1} \text{ mg}_{\text{cat}}^{-1}$  and 11.90% at 0.4 V vs. Ag/AgCl, respectively, whereas the SG conversion rate of the oxidation reaction under the same conditions was 100% and the GA selectivity rate was 96.96% for a 12 hour reaction.

In addition to the previously mentioned research study that used transition metal-based MOFs, main group metal-based MOFs have also been explored as NRR catalysts. In the following year, MIL-100(Al) was utilized as a NRR catalyst by the Ma group.<sup>71</sup> The performance was evaluated in  $\text{N}_2$ -saturated 0.1 M KOH aqueous electrolytes at ambient temperature and pressure. The amount of produced  $\text{NH}_3$ , rate and FE was  $43.15 \mu\text{g h}^{-1} \text{ cm}^{-2} \text{ mg}_{\text{cat}}^{-1}$  and 10.9% at  $-0.7 \text{ V vs. RHE}$ , respectively. The stability of the MIL-100 (Al) catalyst was verified, which revealed that upon the completion of five cycles of the NRR at 177 mV, the  $\text{NH}_3$  production rate and FE were both maintained with insignificant changes. Besides, at a constant overpotential of 177 mV for 10 hours, no observable changes were exhibited by current density.

An approach focusing on functional groups, different from metal sites, was also described. Yin and colleagues utilized both MIL-88B-Fe and  $\text{NH}_2$ -MIL-88B-Fe as electrocatalysts for the NRR.<sup>76</sup> 0.1 M  $\text{Na}_2\text{SO}_4$  aqueous solution was adopted as the electrolyte. The former MOF exhibited an  $\text{NH}_3$  production rate of  $3.575 \times 10^{-11} \text{ mol s}^{-1} \text{ cm}^{-2}$  and a FE of 5.59% at  $-0.25 \text{ V vs. RHE}$ . On the other hand, the latter one featured the highest  $\text{NH}_3$  production rate of  $1.205 \times 10^{-10} \text{ mol s}^{-1} \text{ cm}^{-2}$  with a FE of 5.66% at  $-0.45 \text{ V vs. RHE}$ , which was higher than that of the former. Additionally, the highest FE of  $\text{NH}_2$ -MIL-88B-Fe was 12.45% at 0.05 V vs. RHE. In terms of the selectivity of  $\text{NH}_3$ , no existing  $\text{N}_2\text{H}_4$  was detected during the NRR, which indicated high selectivity.

To achieve more efficient NRR activity, conductive MOFs were explored for this reaction. In a separate study by Jiang, Sun and co-workers,  $\text{Co}_3\text{HHTP}_2$  was loaded on CP and employed as the working electrode with a  $\text{N}_2$ -saturated 0.5 M  $\text{LiClO}_4$  solution as the electrolyte.<sup>77</sup> The NRR performances of  $\text{Co}_3\text{HHTP}_2/\text{CP}$

were evaluated at different potentials and the highest  $\text{NH}_3$  yield rate was  $22.14 \mu\text{g h}^{-1} \text{ mg}_{\text{cat}}^{-1}$  with FE of 3.34% at  $-0.40 \text{ V vs. RHE}$ . The stability and durability of  $\text{Co}_3\text{HHTP}_2/\text{CP}$  were also evaluated through cycling test and time-dependent current density. All the results revealed that  $\text{Co}_3\text{HHTP}_2/\text{CP}$  has adequate stability during the NRR.

For practical application, Liu and colleagues adopted a typical MOF, HKUST-1 as the NRR catalyst.<sup>78</sup> HKUST-1 was dropped on CP and the electrode was named HKUST-1/CP. The highest NRR performance was achieved at  $-0.75 \text{ V vs. RHE}$  with an  $\text{NH}_3$  yield rate of  $46.63 \mu\text{g h}^{-1} \text{ mg}_{\text{cat}}^{-1}$  and a FE of 2.45%. Time-dependent experiments evidenced a nearly linear relation between the amount of  $\text{NH}_3$  generated and time, and no trace of the by-product  $\text{N}_2\text{H}_4$  was detected at any potential.

Furthermore, another investigation of how the amount of metal precursors affects catalytic activity was conducted. In 2021, Jing, Zhang and colleagues reported the Cu-MOF and Ce-MOF grown on the surface of copper mesh (hereinafter Cu@Cu-MOF and Cu@Ce-MOF) and employed as NRR catalysts.<sup>79</sup> Regarding Ce-MOFs, three kinds of MOFs with different amounts of Ce precursors were prepared. The amounts of  $\text{Ce}(\text{NO}_3)_3 \cdot 6\text{H}_2\text{O}$  used for synthesizing Ce-MOF-1, Ce-MOF-2 and Ce-MOF-3 were 20 mg, 60 mg and 300 mg, respectively. All NRR experiments were conducted by utilizing 0.1 M KOH aqueous solution as the electrolyte. The results indicated that the  $\text{NH}_3$  yield and FE were  $10.23 \mu\text{g h}^{-1} \text{ cm}^{-2}$  and 5.12%, respectively at  $-0.2 \text{ V vs. RHE}$ . On the other hand, each of the Ce-MOFs exhibited higher activity than Cu-MOFs; Cu@Ce-MOF-2 illustrated the highest  $\text{NH}_3$  yield ( $14.83 \mu\text{g h}^{-1} \text{ cm}^{-2}$ ) and FE (10.81%) among the three Cu@Ce-MOFs at  $-0.2 \text{ V vs. RHE}$  (Fig. 4b). Additionally, Cu@Ce-MOF-2 possessed high stability during nine cycles. Besides, Cu@Ce-MOF-2 showed selectivity towards  $\text{NH}_3$ , which was indicated by the absence of  $\text{N}_2\text{H}_4$  detection.

As part of fundamental research, how solvent conditions affect the NRR catalytic activity of MOFs was evaluated. Chen, Duan and co-workers leveraged the 2D In-MOF for evaluating NRR activity in various pH electrolytes.<sup>80</sup> The highest  $\text{NH}_3$  yield rates at  $-0.5 \text{ mA cm}^{-2}$  were 24.70, 25.80, 64.73, 79.20 and  $71.58 \mu\text{g h}^{-1} \text{ mg}^{-1}$  corresponding to pH values of 1, 2, 7, 12 and 14, respectively. The FEs were calculated to be 6.72, 7.50, 12.23, 14.98 and 13.54% at pH 1, 2, 7, 12 and 14, respectively, in which the former two were measured at  $-0.25 \text{ mA cm}^{-2}$  and others were measured at  $-0.5 \text{ mA cm}^{-2}$ . The results unveiled the best NRR performance at pH 12 among the various pH experimental conditions. Furthermore, the In-MOF exhibited superb stability even when it was exposed to acid and alkaline solutions. The theoretical investigation showed that the reaction occurred on In atoms, and the process followed an enzymatic pathway, which was accomplished by the Gibbs free energy changes. Furthermore, the calculation results showed that the rate-determining step in the NRR was the first  $\text{NH}_3$  generation step.

Several studies have demonstrated the improvement in catalytic activity upon creating defects in the MOF structure. In 2022, the Yin group harnessed defective UiO-66- $\text{NH}_2$  to adsorb  $\text{O}_2$  radicals for the NRR.<sup>81</sup> The best NRR performance in terms of the  $\text{NH}_3$  yield rate and FE with UiO-66- $\text{NH}_2$  was  $\sim 2.071 \times$





$10^{-10}$  mol s<sup>-1</sup> cm<sup>-2</sup> and ~85.21%, respectively, at -0.39 V vs. RHE in N<sub>2</sub>-saturated 0.1 M Na<sub>2</sub>SO<sub>4</sub>. Besides, UiO-66-NH<sub>2</sub> was used in the NRR for 6 cycles, indicative its high stability during the course of this reaction. The high value of FE is attributable to the Zr-OO' sites which are formed by exposed Zr atoms, adsorbed O<sub>2</sub> radicals and -NH<sub>2</sub> functional groups stabilizing the Zr-OO' sites.

A study on defective MOFs was reported by the Yin group as well. They also utilized the same MOF, UiO-66, that was made defective by implementing HPMo (hereinafter UiO-66-xHPMo, where x represents the ratio of Zr and Mo: 0.5, 1, 2 and 3) as an electrocatalyst for the NRR.<sup>82</sup> UiO-66-xHPMo presented a four-fold enhancement in NRR activity with a maximum NH<sub>3</sub> yield rate of 36.61 μg h<sup>-1</sup> mg<sub>cat</sub><sup>-1</sup> relative to pristine UiO-66. However, regarding FE, UiO-66 displayed the best results with a FE of 35.76%, which suggested that the MOF defects decreased the proton conductivity thereby enhancing the charge transfer resistance. Regarding UiO-66-xHPMo, UiO-66-2HPMo illustrated the best NRR activity with an NH<sub>3</sub> yield rate of 36.61 μg h<sup>-1</sup> mg<sub>cat</sub><sup>-1</sup> and FE of 31.09% at -0.3 V vs. RHE (Fig. 4d). The N<sub>2</sub>H<sub>4</sub> by-product yield during the NRR was also measured to assess the selectivity, and the highest N<sub>2</sub>H<sub>4</sub> yield was 0.04 μg h<sup>-1</sup> mg<sub>cat</sub><sup>-1</sup> at -0.1 V vs. RHE. Furthermore, the current density at -0.3 V vs. RHE remained almost unchanged for 48 h, and UiO-66-2HPMo showed no obvious changes after five catalytic runs, demonstrating the adequate durability of UiO-66-2HPMo.

Recently, another defect-based MOF study for the NRR has been carried out. Liu, Yan and colleagues introduced a defective Al-Fum MOF, which was deposited on CP for the NRR.<sup>83</sup> The concentration of K<sub>2</sub>SO<sub>4</sub> as the electrolyte was selected as 0.4 M. Under this condition, the highest NH<sub>3</sub> yield rate and FE of Al-Fum MOF at -0.15 V vs. RHE were 53.9 μg h<sup>-1</sup> mg<sub>cat</sub><sup>-1</sup> and 32.9%, respectively. To corroborate the importance of defective sites in the Al-Fum MOF, the NRR performances of pristine and defective Al-Fum MOF were compared under the same conditions, which indicated noticeably lower activity of the former (NH<sub>3</sub> yield rate: 13.2 μg h<sup>-1</sup> mg<sub>cat</sub><sup>-1</sup>, FE: 11.8%) than the latter. To validate the stability of the defective Al-Fum MOF, ten NRR cycles were conducted which demonstrated that the NH<sub>3</sub> yield rate and FE were maintained, suggestive of its superb stability. The DFT calculations deciphered the pivotal role of defective Al sites in activating N<sub>2</sub>, which facilitated the NRR process.

Research studies also focused on exploring the relationship between the symmetry of connections between metal sites and linkers and catalytic activity. Zhou, Lee and co-workers decoded the effect of symmetry-breaking in three MOFs on the NRR activity by enabling the adsorption of N<sub>2</sub>.<sup>84</sup> The Zn-N<sub>2</sub>S<sub>2</sub>-MOF presented the highest NH<sub>3</sub> yield rate of 25.07 ± 1.57 μg h<sup>-1</sup> cm<sup>-2</sup> and a FE of 44.57 ± 2.79% at -0.3 V vs. RHE (Fig. 4e) and it was further characterized by XPS, X-ray absorption near-edge structure (XANES) and extended X-ray absorption fine structure (EXAFS). The study highlighted that increasing the number of S atoms around Zn-sites enhances the Zn electron density because of delocalized electrons donated by S, which resulted in high NRR activities by suppressing the HER. Additionally, the importance of symmetry-breaking for the ORR and CRR in the three MOFs was explored.

#### 4.2. Multiple metal MOFs for the NRR

MOFs constructed using multiple kinds of metal species have been widely reported and exhibit synergistic effect with superior catalytic activity compared to single metal MOFs. In 2020, Yan *et al.* reported bimetallic MOFs, Co<sub>x</sub>Fe-MOF, utilized for the OER and NRR.<sup>85</sup> In terms of the NRR, the performance of the Co<sub>3</sub>Fe-MOF was evaluated under ambient conditions with 0.1 M KOH electrolyte. The best yield rate of NH<sub>3</sub> produced and FE were 8.79 μg h<sup>-1</sup> mg<sub>cat</sub><sup>-1</sup> and 25.64%, respectively, at -0.2 V vs. RHE. The Co<sub>3</sub>Fe-MOF also revealed outstanding stability after 4 cycles, each cycle lasting for 2 hours.

The study on bimetallic MOFs containing Fe was further investigated in another study by Chen, Zhao and co-workers employing a zero-dimensional Ni and Fe-based bimetallic MOF, NiFe-MOF, as the NRR catalyst.<sup>86</sup> The NRR performance of the NiFe-MOF was investigated with 0.1 M NaHCO<sub>3</sub> aqueous electrolyte at ambient temperature and pressure. The NH<sub>3</sub> production rate was obtained to be 9.3 μg h<sup>-1</sup> mg<sub>cat</sub><sup>-1</sup> and the FE was 11.5% at -347 mV vs. RHE. In order to examine the reaction pathway in detail, density functional theory (DFT) calculations were conducted. The nitrogen molecules were physically adsorbed onto the metal sites, which worked as active sites, and the reaction proceeded through the associative pathway. Furthermore, the analysis of the minimum-energy pathway indicated that the Ni-MOF and Fe-MOF showcased the highest Gibbs free energy during the release of the first NH<sub>3</sub> molecule, making it the rate-limiting step. On the other hand, in the case of the NiFe-MOF, the energy during NH<sub>3</sub> desorption decreased as compared to the previous stage. This result demonstrated that MOFs constructed using multiple metals allow for the control of Gibbs free energy during the reaction step.

The Yin group reported the UiO-Zr-Ti MOF, prepared by post-synthetic metal exchange on parent UiO-66-NH<sub>2</sub> which led to substitution of some Ti clusters for Zr clusters, which displayed NRR activity in 0.1 M Na<sub>2</sub>SO<sub>4</sub> electrolyte.<sup>87</sup> UiO-Zr-Ti synthesized in an oven for 5 days showed the highest NH<sub>3</sub> production rate of 1.16 ± 0.058 × 10<sup>-10</sup> mol s<sup>-1</sup> cm<sup>-2</sup>, and the highest FE was 80.36 ± 4.23% at -0.3 V vs. RHE. From the viewpoint of product selectivity, N<sub>2</sub>H<sub>4</sub> which is the by-product of the NRR was only 5.8 × 10<sup>-13</sup> mol s<sup>-1</sup> cm<sup>-2</sup>, which was appreciably lower than the NH<sub>3</sub> production rate.

There is also a further study that changed the ratio of the number of metals of polyoxometalate (POM)-based MOFs. Wang, Ma, Kan and co-workers reported POM-based MOFs, namely, Fe<sub>x</sub>Co<sub>y</sub>MOF-P<sub>2</sub>W<sub>18</sub> which were employed as catalysts for the NRR.<sup>88</sup> Fe<sub>x</sub>Co<sub>y</sub>MOF-P<sub>2</sub>W<sub>18</sub> was prepared by changing the Fe/Co ratio and named accordingly as CoMOF-P<sub>2</sub>W<sub>18</sub>, FeCo<sub>2</sub>-MOF-P<sub>2</sub>W<sub>18</sub>, FeCoMOF-P<sub>2</sub>W<sub>18</sub>, Fe<sub>2</sub>CoMOF-P<sub>2</sub>W<sub>18</sub> and FeMOF-P<sub>2</sub>W<sub>18</sub>. The results demonstrated that FeCoMOF-P<sub>2</sub>W<sub>18</sub> outperformed other MOFs with an NH<sub>3</sub> yield rate and FE of 47.04 μg h<sup>-1</sup> mg<sub>cat</sub><sup>-1</sup> and 31.76% at -0.4 V vs. RHE, respectively. The NRR performance of FeCoMOF-P<sub>2</sub>W<sub>18</sub> was also compared with that of pristine FeCoMOF and the former was found to be notably higher than the latter (Fig. 4c). Furthermore, pure P<sub>2</sub>W<sub>18</sub> did not show NRR activities, which indicated that the



NRR activities of bimetallic MOFs were greatly improved. During the NRR,  $N_2H_4$  was not identified, which indicated the high selectivity of  $NH_3$ . To substantiate the recyclability of  $Fe_xCo_yMOF-P_2W_{18}$ , cycling tests were performed and the current densities during the NRR process were measured. The results of cycling tests revealed that  $NH_3$  yield rates and FEs remained stable over five cycles. No detectable changes in current densities were found during the 12 hours of the NRR experiment.

CoFe-MIL-88A was *in situ* grown on 2D  $V_2CT_x$  MXene (hereinafter CoFe-MIL-88A/ $V_2CT_x$ ) by Li, Zhang and co-workers for use as a NRR electrocatalyst.<sup>89</sup> CoFe-MIL-88A/ $V_2CT_x$  displayed a  $NH_3$  yield rate and FE of  $29.47 \mu g h^{-1} mg_{cat}^{-1}$  at  $-0.3 V$  vs. RHE and 28.86% at  $-0.1 V$  vs. RHE, respectively. These results were far superior to those for pristine CoFe-MIL-88A and  $V_2CT_x$ , and the  $NH_3$  was entirely derived from  $N_2$ . The selectivity of  $NH_3$  was also validated by assessing the amount of  $N_2H_4$  production and during eNRR measurement; no  $N_2H_4$  was identified. The high NRR activity can be ascribed to the coating of CoFe-MIL-88A by  $V_2CT_x$ , thereby rendering the surface hydrophobic which inhibited the competitive HER pathway. The MOF/MXene composites also indicated high stability during electrocatalytic tests.

Research focusing on metal single atoms within the organic linker of multiple metal MOFs was also reported. Gao, Zhang and colleagues reported the NRR activities of Fe-TCPP, Co-TCPP and Zn-TCPP MOFs that changed with differing metal ions residing inside the porphyrin macrocycle.<sup>90</sup> 0.1 M HCl was utilized as electrolyte. The  $NH_3$  production performance and FE of Fe-TCPP, Co-TCPP and Zn-TCPP MOFs were  $44.77 \mu g h^{-1} mg_{cat}^{-1}/16.23%$ ,  $28.3 \mu g h^{-1} mg_{cat}^{-1}/11.58%$  and  $19.59 \mu g h^{-1} mg_{cat}^{-1}/6.37%$ , respectively. Each performance was higher than that of CP, and Fe-TCPP showcased the best NRR performance among all MOFs reported before this study. DFT calculation results suggested the interaction strength and bond distance between nitrogen molecules and each metal atom, revealing that the activation state of nitrogen molecules is favorable in the order of Fe-TCPP, Co-TCPP, and Zn-TCPP. In terms of the NRR pathway, the calculation also indicated that only Fe-TCPP followed the associative distal pathway, and the others proceeded *via* the associative alternating pathway. This difference was caused by the bond distance between nitrogen molecules and active sites and the degree of activation. The reaction rate was determined by the initial step of hydrogenation of the nitrogen molecules, and the Gibbs free energy for this step is the lowest for Fe-TCPP and highest for Zn-TCPP, which was consistent with the experimental results.

Another research study on MOFs including porphyrin linkers by Solla-Gullón, Tatay, Marti-Gastaldo and colleagues probed the NRR activities with the PCN-224 family of Zr cluster-based MOF electrocatalysts.<sup>91</sup> PCN-224 indicated brilliant stability under NRR conditions. Furthermore, the MOFs constructed with  $Co^{2+}$ ,  $Ni^{2+}$  and  $Cu^{2+}$ -metalated porphyrin linkers exhibited the FEs of 11.4, 32.3 and 21.7% at  $-0.04 V$  vs. RHE, respectively. However, PCN-224-Ni was found to elute during the NRR, which was suggested by ICP-analysis. Hence, PCN-224-Ni faced a stability issue. Moreover, fluorine was introduced into PCN-

224-Ni to compare the importance of functional groups in the porphyrin linker. As a result, FE was improved from 32.3% to 34.5% at  $-0.04 V$  vs. RHE and the  $NH_3$  yield rate was  $0.9 \mu g h^{-1} mg_{cat}^{-1}$ . From the viewpoint of stability, the durability of PCN-224-Ni(F) was enhanced and during the electrocatalytic reaction for 24 h, the morphology of the crystal did not show any obvious change.

### 4.3. MOF composites for the NRR

A lot of research on composite materials including MOFs has been carried out recently. In 2018, the Ling group deposited silver nanocubes onto the gold electrode followed by covering this with the zeolite imidazole framework, ZIF-71 (hereinafter Ag-Au@ZIF) (Fig. 3a).<sup>92</sup> The NRR performance was assessed under ambient conditions (298 K and 1 bar) using a  $LiCF_3SO_3$  electrolyte and  $\sim 1$  wt% ethanol THF-solution. The average efficiency of producing ammonia was approximately  $10 pmol cm^{-2} s^{-1}$  and FE was  $18 \pm 4%$  at  $-2.9 V$ . Furthermore, this Ag-Au@ZIF electrode presented a turnover number and frequency improved by more than four times, and an impressive NRR selectivity of about 90% was attained. These high performances are ascribed to the ZIF coating that possesses superhydrophobicity which suppresses the HER and high gas adsorption capacity to concentrate  $N_2$ .

In the following year, Li, Du and colleagues utilized a different zeolite imidazole framework, ZIF-8, to encapsulate NPG.<sup>96</sup> The performance of this composite catalyst (termed NPG@ZIF-8) was examined by using a  $N_2$ -saturated 0.1 M  $Na_2SO_4$  water solution as the electrolyte. When the experiment was carried out at  $-0.8 V$  vs. RHE, the  $NH_3$  production was as high as  $28.7 \pm 0.9 \mu g h^{-1} cm^{-2}$ . On the other hand, the highest FE obtained was 44% and the selectivity of ammonia was 98% at  $-0.6 V$  vs. RHE (Fig. 4a). NPG@ZIF-8 also displayed brilliant stability even if it was exposed to a constant potential of  $-0.6 V$  vs. RHE for 12 h, showing only a marginal decrease in current density.

ZIF-71 composite catalysts with different catalysts incorporated inside have also been presented. A study by Ling *et al.* reported the use of ZIF-71 for encapsulating PtNSs on Au electrodes (referred to as Pt/Au@ZIF).<sup>98</sup> The electrolyte was an anhydrous THF solution containing  $LiCF_3SO_3$  with 1 wt% ethanol serving as a proton source. First, PtNS size dependence was confirmed, and the results showcased that the smaller PtNSs ranging from 60 nm to 231 nm exhibited higher FE and  $NH_3$  yield rates. Second, the NRR performance was evaluated by utilizing 60 nm Pt/Au@ZIF at various potentials from  $-1.7 V$  to  $-3.3 V$  vs. Ag/AgCl. Furthermore, the results revealed that the highest FE and  $NH_3$  yield rate were  $44.8 \pm 4.2%$  and  $161.9 \pm 16.7 \mu g h^{-1} mg_{cat}^{-1}$ , respectively under ambient conditions at  $-2.9 V$  vs. Ag/AgCl. Pt/Au@ZIF also demonstrated a FE of over 40% and an ammonia yield rate of over  $130 \mu g h^{-1} mg_{cat}^{-1}$  across a wide range of potentials. They also compared Pt/Au@ZIF with Pt/Au, Au@ZIF and dcim-Pt/Au, which was covered with monolayer of linker molecules (dcim) and the results displayed that Pt/Au@ZIF possesses the best NRR activities.



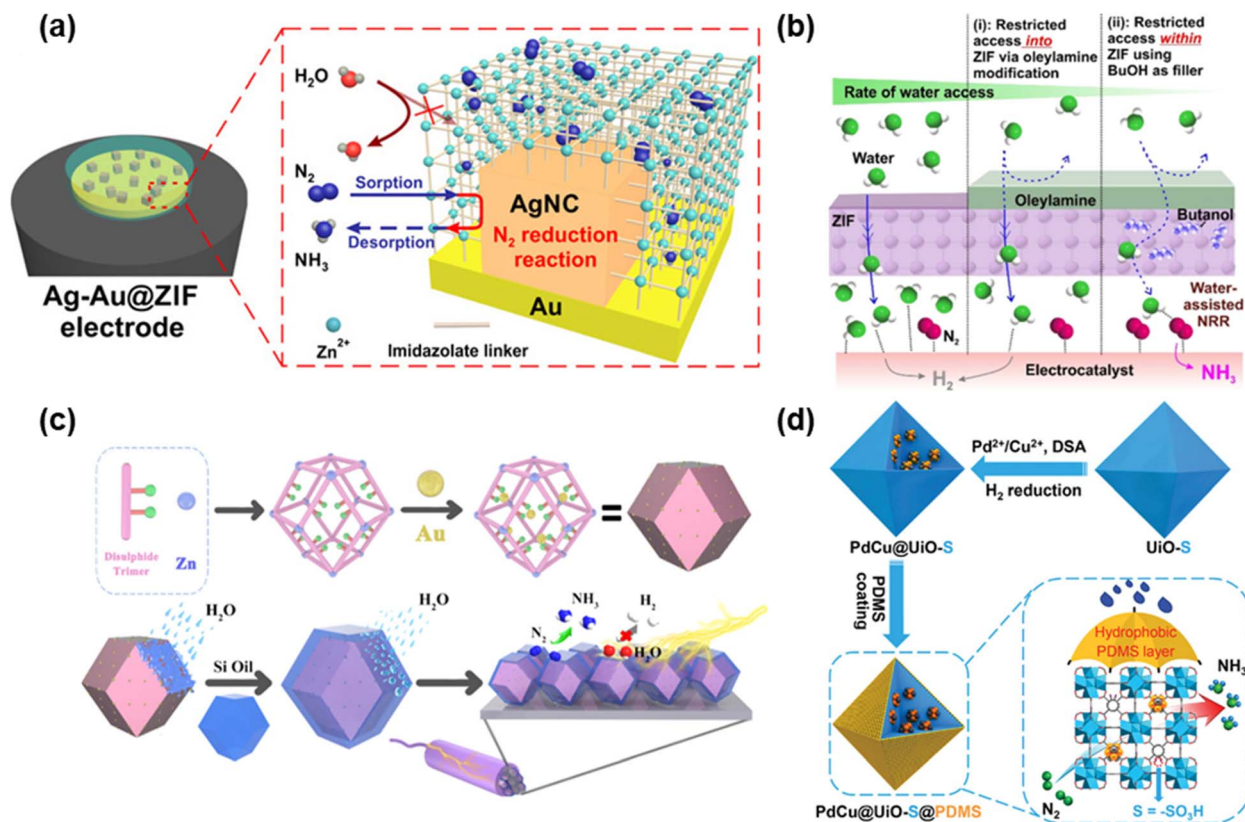


Fig. 3 Methods for introducing hydrophobicity: (a) schematic illustration of Ag nanocubes deposited on the Au electrode followed by covering with ZIF-71. Adapted with permission from ref. 92. Copyright 2018, The American Association for the Advancement of Science. (b) M@ZIF-Oam electrocatalyst prepared by utilizing ZIF-71 for coating the metallic electrocatalysts followed by modifying OAM to impart hydrophobicity. Adapted with permission from ref. 93. Copyright 2020, American Chemical Society. (c) HT Au@MOF prepared by inserting AuNPs as guests inside the MOF pores followed by covering the MOF surface with organosilicon. Adapted with permission from ref. 94. Copyright 2021, Elsevier B.V. (d) PdCu@UiO-S@PDMS prepared by encapsulating PdCu NPs into the pores of UiO-S followed by coating with hydrophobic PDMS. Reprinted with permission from ref. 95. Copyright 2023, Wiley-VCH GmbH.

Apart from MOFs, another method that enhanced hydrophobicity was also endeavored. A study by Ling *et al.* utilized ZIF-71 for coating the metallic electrocatalysts and then modified OAm to impart hydrophobicity (denoted as M@ZIF-Oam) (Fig. 3b).<sup>93</sup> Additionally, butanol molecules were added into ZIF-71 to limit the amount of accessible water molecules. First, CV measurements of M@ZIF-Oam with butanol, M@ZIF with butanol, and M@ZIF-Oam without butanol were conducted with dry THF, trifluoromethanesulfonate and 1 wt% butanol as electrolytes including 0.25 wt% water under  $N_2$  and Ar-bubbling. M@ZIF-Oam with butanol showed a reduction peak at  $-2.5$  V vs. Ag/AgCl, indicating NRR activity. On the other hand, other two electrodes exhibited no peak at  $-2.5$  V, and the peak at  $-1.3$  V confirmed the occurrence of the HER. The results revealed that both coating with OAm and adding butanol were crucial for adsorbing  $N_2$  and adjusting the interaction of water molecules with the electrocatalyst. Second, the NRR of M@ZIF-Oam and M@ZIF was performed at  $-2.9$  V for 6 hours under  $N_2$ -bubbling upon varying the amount of added water. The highest ammonia yield rate and FEs in the presence of water between 0 wt% and 0.25 wt% were  $45.3 \pm 2.9 \mu\text{g h}^{-1} \text{mg}^{-1}$  and 18%, respectively, in the presence of 0.1 wt% water. Both values were

by far higher than those observed in the absence of water. In contrast to these results, the NRR performance of uncoated M@ZIF illustrated the best  $NH_3$  production rate and FE were  $21 \pm 7.2 \mu\text{g h}^{-1} \text{mg}^{-1}$  and  $5 \pm 0.2\%$ , respectively, under no-water conditions, which substantiated the necessity of hydrophilicity. On another note, the stability of M@ZIF-Oam was confirmed by monitoring the values of current density at  $-2.9$  V during 80 cycles, and there was relatively no change in this value.

In 2022, the Du group prepared a 3D MOF by using Zn(II) ions and 3,3'-bis(mercapto)biphenyl-*p,p'*-dicarboxylic acid, followed by inserting AuNPs as guests inside the MOF pores.<sup>94</sup> Moreover, to enhance hydrophobicity, the surface of the MOF was covered with organosilicon (PMX-200-500CS), and this substance was named HT Au@MOF (Fig. 3c). The NRR performance of HT Au@MOF achieved the highest  $NH_3$  yield and FE of  $49.5 \mu\text{g h}^{-1} \text{mg}_{\text{cat}}^{-1}$  and 60.9%, respectively, at  $-0.3$  V vs. RHE. The high selectivity of  $NH_3$  was also established by the absence of  $N_2H_4$  detection. The performance of HT Au@MOF surpassed that of Au@MOF, and the LSV tests under Ar-saturation also indicated that the current density of HT Au@MOF was strikingly lower than that of Au@MOF, which highlighted that coating organosilicon could suppress the HER.



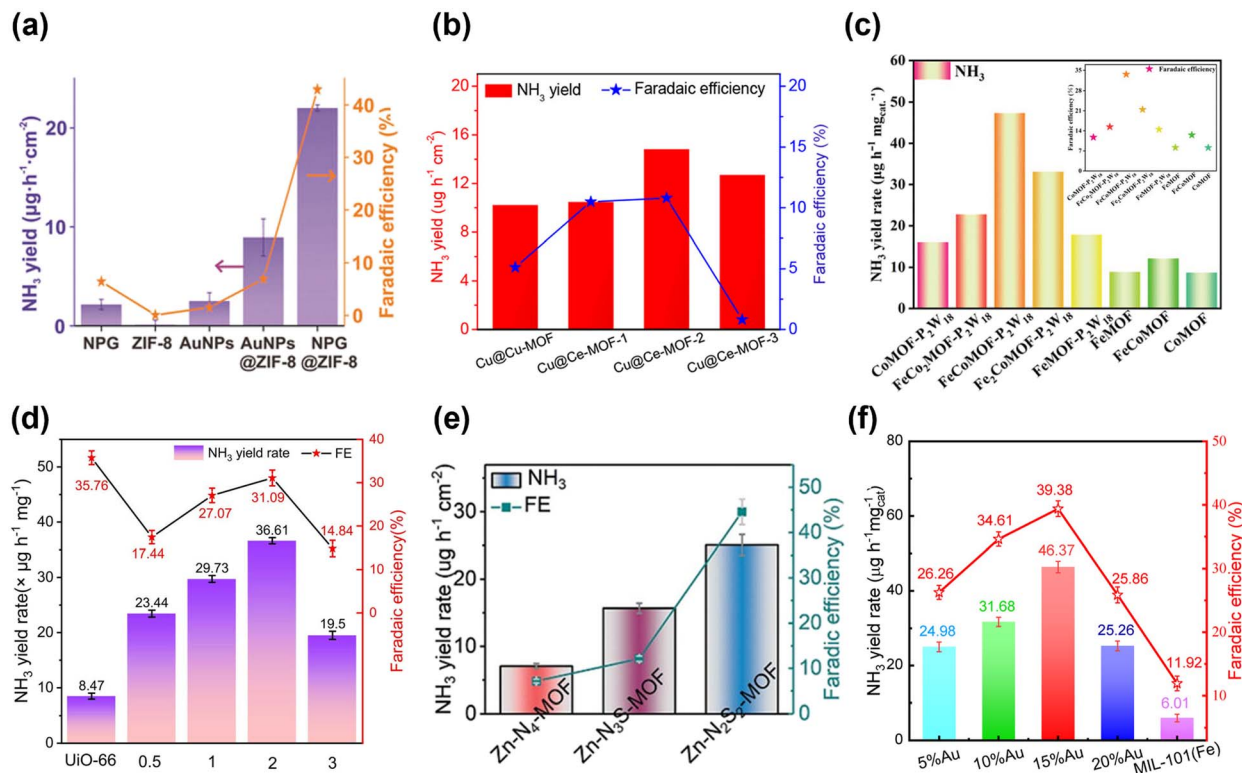


Fig. 4 Catalytic performances of different electrocatalysts in terms of the NH<sub>3</sub> yield rate and FE: (a) NPG encapsulated into ZIF-8 (NPG@ZIF-8). Adapted with permission from ref. 96. Copyright 2019, John Wiley and Sons. (b) Cu-MOF and Ce-MOF grown on the surface of copper mesh (Cu@Cu-MOF and Cu@Ce-MOF). Adapted with permission from ref. 79. Copyright 2021, American Chemical Society. (c) Polyoxometalate-based MOFs (Fe<sub>x</sub>Co<sub>y</sub>MOF-P<sub>2</sub>W<sub>18</sub> and Fe<sub>x</sub>Co<sub>y</sub>MOF). Adapted with permission from ref. 88. Copyright 2023, Wiley-VCH GmbH. (d) UiO-66 that was made defective by introducing HPMo (UiO-66-xHPMo). Adapted with permission from ref. 82. Copyright 2024, Elsevier B.V. (e) Zn-N<sub>2</sub>S<sub>2</sub>-MOF, Zn-N<sub>3</sub>S-MOF, and Zn-N<sub>4</sub>-MOF. Adapted with permission from ref. 84. Copyright 2023, Wiley-VCH GmbH. (f) xAu/MIL-101(Fe), x = 5, 10, 15 or 20%. Adapted with permission from ref. 97. Copyright 2024 Wiley-VCH GmbH.

Furthermore, they implemented other three MOFs (DTU-67, 2,5-TP and MIL-101-SO<sub>3</sub>) in the same reaction. The experimental findings revealed that there is a negative correlation between the size of AuNPs and the NRR activities. The size of AuNPs that were encapsulated into MOFs in ascending order was HT Au@MOF, HT Au@DTU-67, HT Au@2,5-TP and HT Au@MIL-101-SO<sub>3</sub>. Meanwhile, the order of NRR activities in these materials followed HT Au@MOF > HT Au@DTU-67 > HT Au@2,5-TP > HT Au@MIL-101-SO<sub>3</sub>. The reaction was carried out on the surface of AuNPs, and the mechanism confirmed that the reaction progressed *via* the associative distal pathway because no N<sub>2</sub>H<sub>4</sub> was observed. The stability of HT Au@MOF was also confirmed for six cycles of the NRR at -0.3 V *vs.* RHE with virtually no change in the NH<sub>3</sub> yield rate and FE after the sixth catalytic run.

The Jiang group encapsulated PdCu NPs into the pores of UiO-S followed by coating with PDMS (hereinafter PdCu@UiO-S@PDMS) and used it as catalyst for the NRR.<sup>95</sup> The PDMS coating endowed PdCu@UiO-S with hydrophobicity (Fig. 3d). PdCu@UiO-S@PDMS exhibited the highest NH<sub>3</sub> yield rate of 20.24 μg h<sup>-1</sup> mg<sub>cat</sub><sup>-1</sup> and a FE of 13.16% at -0.25 V *vs.* RHE. Comparative analyses of the performances of PdCu@UiO-S@PDMS, UiO-S@PDMS and Pd@UiO-S@PDMS substantiated

that PdCu NPs functioned as active sites for the NRR. The study revealed that the optimal NRR performance was achieved in the presence of a 10% molar ratio of Cu in CuPd NPs. On another note, the performances of PdCu@UiO-S@PDMS and PdCu@UiO@PDMS were compared to evince the importance of -SO<sub>3</sub>H functional groups, showing the superiority of PdCu@UiO-S@PDMS over PdCu@UiO@PDMS. To assess hydrophobicity, the contact angles of PdCu@UiO-S and PdCu@UiO-S@PDMS were determined to be 2.2° and 137.3°, respectively, which illustrated that coating PDMS enhanced the hydrophobicity, which eventually impeded the HER. Furthermore, PdCu@UiO-S@PDMS featured high selectivity and stability.

The Yin group loaded Au NPs on MIL-101(Fe) to boost its electrocatalytic activity for the NRR.<sup>97</sup> The ratio of AuNPs and MIL-101(Fe) was changed and the compounds were termed xAu/MIL-101(Fe), x = 5, 10, 15 or 20%. Among xAu/MIL-101(Fe), 15%Au/MIL-101(Fe) exhibited the best performance with the highest NH<sub>3</sub> yield rate of 46.37 μg h<sup>-1</sup> mg<sub>cat</sub><sup>-1</sup> and a FE of 39.98% at -0.4 V *vs.* RHE (Fig. 4f). The NRR activity was also inspected by changing the potential, which revealed that the NRR performance was highest at -0.4 V owing to the strongest absorbance intensity at -0.4 V. Au NPs demonstrated high HER



activity but due to the increased  $N_2$  concentration provided by MIL-101(Fe), the NRR activity was dramatically enhanced by hindering the HER pathway.

MOF composites combining MOFs and carbon materials were also explored. A study on MOFs with CNTs for the NRR was reported by Ding *et al.* in the same year.<sup>99</sup> In this contribution, four MOFs (UIO-66, BIT-58, CAU-17 and MIL-101(Fe)) were utilized for inserting CNTs and N-doped CNTs (hereinafter CNT/NCNT@MOF), and all electrical measurements were done in 0.05 M  $H_2SO_4$ . All of the MOF compounds featured markedly superior NRR activities compared to pristine CNTs and NCNTs. From these results, MOFs contributed to hydrophobic suppression of the HER and enrichment of  $N_2$ . On another note, CNT@MOFs preserved their crystallinity after six cycles, which suggested that CNT@MOFs have notable stabilities.

Other MOF and CNT compounds are also utilized as NRR catalysts. Yin and co-workers prepared UiO-66-NH<sub>2</sub> deposited on CNTs (UiO-66-NH<sub>2</sub>/CNT-*X*, where *X* denotes the amount of CNTs used to synthesize the composite: 0.05, 0.10, 0.15 or 0.20 g) and used them as NRR catalysts.<sup>100</sup> A 0.1 M  $Na_2SO_4$  solution was used as the electrolyte and MOF/CNT composites served as working electrodes. All results of the NRR showed that UiO-66-NH<sub>2</sub>/CNT-0.15 achieved the highest  $NH_3$  yield rate of  $1.854 \times 10^{-10} \text{ mol s}^{-1} \text{ cm}^{-2}$  (FE: 37.38%), whereas UiO-66-NH<sub>2</sub>/CNT-0.05 showed the best FE of 45.51% ( $NH_3$  yield rate:  $1.091 \times 10^{-10} \text{ mol s}^{-1} \text{ cm}^{-2}$ ), both at  $-0.3 \text{ V vs. RHE}$ . The amount of  $N_2H_4$  as a by-product of the NRR was also measured by utilizing UiO-66-NH<sub>2</sub>/CNT-0.15, and the highest yield of  $N_2H_4$  was  $2.84 \times 10^{-13} \text{ mol s}^{-1} \text{ cm}^{-2}$  at  $-0.3 \text{ V vs. RHE}$ , which was significantly lower than the amount of  $NH_3$ . To ascertain stability, UiO-66-NH<sub>2</sub>/CNT-0.15 was recycled in chronoamperometric tests 5 times and the MOF/CNT composites demonstrated impressive stability (the relative  $NH_3$  yield rate and FE were 92.97% and 94.89%, respectively, compared with the first measurement). To monitor the reaction pathway, *in situ* ATR-SEIRAS was utilized, and the results confirmed the formation of hydrogenated nitrogen species ( $N_2H_{1-4}$ ) on the MOF/CNT composite surface. From this fact, it was revealed that the pathway follows the associative alternating pathway.

Efforts to improve conductivity have also been made. Ren, Liu and colleagues utilized ZIF-67 that was supported on  $Ti_3C_2$  (denoted as ZIF-67@ $Ti_3C_2$ ) for the NRR.<sup>101</sup> The performance of ZIF-67@ $Ti_3C_2$  was measured in 0.1 M KOH and the highest  $NH_3$  production rate and FE were  $6.52 \mu\text{mol h}^{-1} \text{ cm}^{-2}$  and 20.2%, respectively, at  $-0.4 \text{ V vs. RHE}$ . For comparative analysis, control experiments were also performed with individual ZIF-67 and  $Ti_3C_2$ , which revealed that the  $NH_3$  yields were  $1.61 \mu\text{mol h}^{-1} \text{ cm}^{-2}$  and  $2.77 \mu\text{mol h}^{-1} \text{ cm}^{-2}$  for ZIF-67 and  $Ti_3C_2$ , respectively.

Moreover, composites including MOFs and sulfide materials were also adopted as catalysts for the NRR. A study by the Wang group adopted ZIF-71 for encapsulation of the  $MoS_2$  nanoflower (hereinafter  $MoS_2$ @ZIF-71), which enhanced the NRR activity in comparison to both of the pristine materials.<sup>102</sup> CP covered with  $MoS_2$ @ZIF-71 achieved the highest  $NH_3$  production rate of  $56.69 \mu\text{g h}^{-1} \text{ mg}_{MoS_2}^{-1}$  and the FE was 30.91% at  $-0.2 \text{ V vs. RHE}$ .

These results also highlighted the contributory role of the MOF coating as a hydrophobic barrier to restrain the HER.

Lang and co-workers prepared the MIL-101(Fe)/ $MoS_3$  composite for use as an NRR catalyst.<sup>103</sup> The best NRR performance was achieved with an  $NH_3$  yield rate and FE of  $25.7 \mu\text{g h}^{-1} \text{ mg}_{cat}^{-1}$  and 36.71%, respectively, at  $-0.1 \text{ V vs. RHE}$ , which exceeded those of MIL-101(Fe) ( $9.38 \mu\text{g h}^{-1} \text{ mg}_{cat}^{-1}$  and 13.39%) and  $MoS_3$  ( $0.75 \mu\text{g h}^{-1} \text{ mg}_{cat}^{-1}$  and 0.03%). From the standpoint of the conversion rate from  $N_2$  to  $NH_3$ , MIL-101(Fe)/ $MoS_3$  furnished almost no  $N_2H_4$  by-product from the NRR. Additionally, MIL-101(Fe)/ $MoS_3$  showed outstanding stability during five cycles and electrolysis for 12 h at  $-0.1 \text{ V vs. RHE}$ , which was assessed by X-ray photoelectron spectroscopy (XPS) measurements.

In addition to the composites mentioned before, composites based on MOFs and oxides were also leveraged as electrocatalysts for the NRR. Li, Lin and colleagues prepared ZIF-8 and combined it with  $CeO_2$  nanorods, which were synthesized by calcining Ce-MOF, (hereinafter  $CeO_2$ -ZIF-8), and the  $CeO_2$ -ZIF-8 dispersion was applied to CP and subsequently used as the NRR electrode.<sup>104</sup> The NRR performance showcased the highest  $NH_3$  yield rate and FE of  $2.12 \mu\text{g h}^{-1} \text{ cm}^{-2}$  and 8.41% at  $-0.5 \text{ V vs. RHE}$ , respectively. The stability of  $CeO_2$ -ZIF-8 was validated through recycling tests. After the sixth cycle, the  $NH_3$  yield rate and FE were  $2.10 \mu\text{g h}^{-1} \text{ cm}^{-2}$  (99.06% compared with the first cycle) and 8.21% (97.62% compared with the first cycle), which implied exceptional stability. Furthermore, when the NRR activity was measured, no  $N_2H_4$  by-product could be traced, which confirmed the high selectivity towards  $NH_3$ .

In the preceding discussion, numerous MOFs that have been employed hitherto as electrocatalysts for the NRR have been highlighted. The performance of different MOF electrocatalysts in the NRR is summarized in Table 1. Striving for better NRR activities, scientists not only adopted a diverse range of metals and linkers to construct MOFs but also introduced defects to facilitate accessibility of the active sites. Besides, other materials like CNTs, MXenes, *etc.* have been used to prepare composites with MOFs for synergistic enhancement of electrocatalytic activities. On another note, MOFs have also been utilized as coatings on other electrocatalysts to impart hydrophobicity, thereby suppressing the HER, which is one of the factors impeding the NRR.

#### 4.4. MOF-derived electrocatalysts for the NRR

The stability of pristine MOFs sometimes raises concerns about their utilization as electrocatalysts due to which MOF-derived electrocatalysts have gained prominence. MOF-derived carbons are promising catalysts for the eNRR, attributed to their remarkable surface areas, customizable functionalities and tailorable pore configuration. Wang, Wu and co-workers adopted a ZIF-8-derived disordered and porous N-doped carbon as a catalyst for the eNRR that presented a noteworthy  $NH_3$  generation rate of  $3.4 \times 10^{-6} \text{ mol cm}^{-2} \text{ h}^{-1}$  and a FE of 10.2% at  $-0.3 \text{ V vs. RHE}$  at room temperature and ambient pressure.<sup>105</sup> The  $NH_3$  generation rate reached  $7.3 \times 10^{-6} \text{ mol}$



Table 1 Performance of different MOF electrocatalysts in the NRR

Year	Electrocatalysts	NH <sub>3</sub> yield rate	Potential/current density	Ref.	
2017	MOF (Fe)	$2.12 \times 10^{-9} \text{ mol s}^{-1} \text{ cm}^{-2}$	-1.2 V vs. Ag/AgCl	74	
	MOF (Co)	$1.64 \times 10^{-9} \text{ mol s}^{-1} \text{ cm}^{-2}$	-1.2 V vs. Ag/AgCl	74	
	MOF (Cu)	$1.24 \times 10^{-9} \text{ mol s}^{-1} \text{ cm}^{-2}$	-1.2 V vs. Ag/AgCl	74	
2018	Ag-Au@ZIF	$\sim 10 \text{ pmol s}^{-1} \text{ cm}^{-2}$	-2.9 V vs. Ag/AgCl	92	
2019	NPG@ZIF-8	$28.7 \pm 0.9 \mu\text{g h}^{-1} \text{ cm}^{-2}$	-0.8 V vs. RHE	96	
	JUC-1000/CC	$24.7 \mu\text{g h}^{-1} \text{ mg}_{\text{cat}}^{-1}$	0.4 V vs. Ag/AgCl	75	
2020	Co <sub>3</sub> Fe-MOF	$8.79 \mu\text{g h}^{-1} \text{ mg}_{\text{cat}}^{-1}$	-0.2 V vs. RHE	85	
	NiFe-MOF	$9.3 \mu\text{g h}^{-1} \text{ mg}_{\text{cat}}^{-1}$	-345 mV vs. RHE	86	
	MIL-100(Al)	$43.15 \mu\text{g h}^{-1} \text{ mg}_{\text{cat}}^{-1}$	-0.7 V vs. RHE	71	
	NH <sub>2</sub> -MIL-88B-Fe	$1.205 \times 10^{-10} \text{ mol s}^{-1} \text{ cm}^{-2}$	-0.45 V vs. RHE	76	
	Pt/Au@ZIF	$161.9 \pm 16.7 \mu\text{g h}^{-1} \text{ mg}_{\text{cat}}^{-1}$	-2.9 V vs. Ag/AgCl	98	
	Co <sub>3</sub> (HHTP) <sub>2</sub> /CP	$22.14 \mu\text{g h}^{-1} \text{ mg}_{\text{cat}}^{-1}$	-0.40 V vs. RHE	77	
	HKUST-1/CP	$46.63 \mu\text{g h}^{-1} \text{ mg}_{\text{cat}}^{-1}$	-0.75 V vs. RHE	78	
	M@ZIF-Oam	$45.3 \pm 2.9 \mu\text{g h}^{-1} \text{ mg}_{\text{cat}}^{-1}$	-2.9 V vs. Ag/AgCl	93	
	2021	Cu@Cu-MOF	$10.23 \mu\text{g h}^{-1} \text{ cm}^{-2}$	-0.2 V vs. RHE	79
		Cu@Ce-MOF	$14.83 \mu\text{g h}^{-1} \text{ cm}^{-2}$	-0.2 V vs. RHE	79
CNT@UiO-66		$3.811 \mu\text{g h}^{-1} \text{ mg}_{\text{cat}}^{-1}$	-0.55 V vs. RHE	99	
NCNT@UiO-66		$6.081 \mu\text{g h}^{-1} \text{ mg}_{\text{cat}}^{-1}$	-0.6 V vs. RHE	99	
CNT@BIT-58		$4.135 \mu\text{g h}^{-1} \text{ mg}_{\text{cat}}^{-1}$	-0.45 V vs. RHE	99	
NCNT@BIT-58		$8.108 \mu\text{g h}^{-1} \text{ mg}_{\text{cat}}^{-1}$	-0.45 V vs. RHE	99	
CNT@CAU-17		$11.92 \pm 0.083 \mu\text{g h}^{-1} \text{ mg}_{\text{cat}}^{-1}$	-0.45 V vs. RHE	99	
NCNT@CAU-17		$13.30 \pm 0.01 \mu\text{g h}^{-1} \text{ mg}_{\text{cat}}^{-1}$	-0.45 V vs. RHE	99	
CNT@MIL-101(Fe)		$5.514 \mu\text{g h}^{-1} \text{ mg}_{\text{cat}}^{-1}$	-0.45 V vs. RHE	99	
NCNT@MIL-101(Fe)		$6.97 \mu\text{g h}^{-1} \text{ mg}_{\text{cat}}^{-1}$	-0.45 V vs. RHE	99	
Fe-TCPP		$44.77 \mu\text{g h}^{-1} \text{ mg}_{\text{cat}}^{-1}$	-0.3 V vs. RHE	90	
Co-TCPP		$28.3 \mu\text{g h}^{-1} \text{ mg}_{\text{cat}}^{-1}$	-0.3 V vs. RHE	90	
Zn-TCPP		$19.59 \mu\text{g h}^{-1} \text{ mg}_{\text{cat}}^{-1}$	-0.3 V vs. RHE	90	
UiO-Zr-Ti		$1.16 \pm 0.058 \times 10^{-10} \text{ mol s}^{-1} \text{ cm}^{-2}$	-0.3 V vs. RHE	87	
ZIF-67@Ti <sub>3</sub> C <sub>2</sub>		$6.52 \mu\text{mol h}^{-1} \text{ cm}^{-2}$	-0.4 V vs. RHE	101	
MoS <sub>2</sub> @ZIF-71		$56.69 \mu\text{g h}^{-1} \text{ mg}_{\text{MoS}_2}^{-1}$	-0.2 V vs. RHE	102	
2D In-MOF	$79.20 \mu\text{g h}^{-1} \text{ mg}_{\text{cat}}^{-1}$	-0.5 mA cm <sup>-2</sup>	80		
2022	HT Au@MOF	$49.5 \mu\text{g h}^{-1} \text{ mg}_{\text{cat}}^{-1}$	-0.3 V vs. RHE	94	
	Defective UiO-66-NH <sub>2</sub>	$\sim 2.071 \times 10^{-10} \text{ mol s}^{-1} \text{ cm}^{-2}$	-0.39 V vs. RHE	81	
	MIL-101(Fe)/MoS <sub>3</sub>	$25.7 \mu\text{g h}^{-1} \text{ mg}_{\text{cat}}^{-1}$	-0.1 V vs. RHE	103	
	CeO <sub>2</sub> -ZIF-8	$2.12 \mu\text{g h}^{-1} \text{ cm}^{-2}$	-0.5 V vs. RHE	104	
2023	FeCoMOF-P2W18	$47.04 \mu\text{g h}^{-1} \text{ mg}_{\text{cat}}^{-1}$	-0.4 V vs. RHE	88	
	PdCu@UiO-S@PDMS	$20.24 \mu\text{g h}^{-1} \text{ mg}_{\text{cat}}^{-1}$	-0.25 V vs. RHE	95	
	UiO-66-NH <sub>2</sub> /CNT-0.15	$1.854 \times 10^{-10} \text{ mol s}^{-1} \text{ cm}^{-2}$	-0.3 V vs. RHE	100	
2024	UiO-66-2HPMO	$36.61 \mu\text{g h}^{-1} \text{ mg}_{\text{cat}}^{-1}$	-0.3 V vs. RHE	82	
	Defective Al-Fum	$53.9 \mu\text{g h}^{-1} \text{ mg}_{\text{cat}}^{-1}$	-0.15 V vs. RHE	83	
	Zn-N2S2-MOF	$25.07 \pm 1.57 \mu\text{g h}^{-1} \text{ cm}^{-2}$	-0.3 V vs. RHE	84	
	15% Au/MIL-101(Fe)	$46.37 \mu\text{g h}^{-1} \text{ mg}_{\text{cat}}^{-1}$	-0.4 V vs. RHE	97	
	CoFe-MIL-88A/V2CTx	$29.47 \mu\text{g h}^{-1} \text{ mg}_{\text{cat}}^{-1}$	-0.3 V vs. RHE	89	
PCN-224-Ni(F)	$0.9 \mu\text{g h}^{-1} \text{ mg}_{\text{cat}}^{-1}$	-0.04 V vs. RHE	91		

cm<sup>-2</sup> h<sup>-1</sup> upon raising the temperature to 60 °C. N-codoped porous carbon with other heteroatoms such as P, B and S also gained attention as efficient NRR electrocatalysts. A study by Song *et al.* demonstrated that N, P co-doped carbon obtained from MOF-5 through pyrolysis served as a highly efficient NRR electrocatalyst that gave NH<sub>3</sub> and N<sub>2</sub>H<sub>4</sub>·H<sub>2</sub>O yields of 1.08 and  $5.77 \times 10^{-4} \mu\text{g h}^{-1} \text{ mg}_{\text{cat}}^{-1}$ , respectively, at -0.1 V vs. RHE.<sup>106</sup> In a similar study by Wang *et al.*, a N, P co-doped carbon prepared by controlling the competition between the N source (ZIF-8) and P source (triphenylphosphine) demonstrated its effectiveness as an NRR electrocatalyst with an impressive NH<sub>3</sub> yield of  $33.02 \mu\text{g h}^{-1} \text{ mg}_{\text{cat}}^{-1}$  and a FE of 7.19% at -0.3 V vs. RHE.<sup>107</sup> MOF-derived single metal atom catalysts also garnered significant attention as NRR electrocatalysts. A study by Si, Zeng and colleagues reported Ru single atoms distributed on

N-doped carbon developed by pyrolyzing a Ru-containing derivative of ZIF-8 that achieved a superb NH<sub>3</sub> yield of  $120.9 \mu\text{g h}^{-1} \text{ mg}_{\text{cat}}^{-1}$  and a FE of 29.6% at -0.2 V vs. RHE.<sup>108</sup> Luo, Tang, Liu and colleagues presented an Fe single atom catalyst developed from bimetallic Fe/Zn ZIF-8 through carbonization and etching.<sup>109</sup> The electrocatalyst displayed an NH<sub>3</sub> generation rate of  $62.9 \pm 2.7 \mu\text{g h}^{-1} \text{ mg}_{\text{cat}}^{-1}$  and a FE of  $18.6 \pm 0.8\%$ , respectively. In addition, metal nanoparticles confined in MOF derived-carbon rods also displayed their efficiency as NRR electrocatalysts. A study by Zheng, Du, Sun and co-workers showcased Bi nanoparticles confined in carbon rods (Bi NPs@CRs), prepared through thermal annealing of a Bi-MOF precursor, which delivered an NH<sub>3</sub> production rate of  $20.80 \mu\text{g h}^{-1} \text{ mg}_{\text{cat}}^{-1}$  and a FE of 11.50% at -0.60 and -0.55 V vs. RHE, respectively.<sup>110</sup>



## 5. Future directions and challenges

Following is the mainstay for future studies on MOFs as electrocatalysts for the NRR.

### 5.1. Durability

In electrocatalytic applications, durability is a pivotal parameter for any material platform and the same pertains to MOFs as well. When MOFs are utilized as heterogeneous electrocatalysts supported onto electrodes for the NRR, it is imperative that the MOF should not dissolve in the electrolyte. This leakage can be assessed by detecting the metal ions that constitute the MOFs in the post-reaction electrolyte by conducting some measurements such as ICP-MS. Besides, the electrochemical stability can be evaluated by monitoring changes during prolonged constant voltage and its recyclability through the same reaction. Moreover, confirming the structure and state of MOFs after use as electrocatalysts *via* powder X-ray diffraction (PXRD) analysis for validating the retention of the crystalline structure, electron microscopy for examining the morphology, XPS and XAFS for observing the oxidation states is crucial to substantiate its long-term operational capacity.

### 5.2. Mechanism

A thorough comprehension of heterogeneous electrocatalytic NRR mechanisms can provide deeper insights into designing new MOF electrocatalysts. Nevertheless, the details and specifics of heterogeneous electrochemistry in most literature studies are insufficient. To accomplish this, *in situ* and *operando* monitoring of intermediates and transition states in heterogeneous electrocatalysis might elucidate the chemistry underpinning it. It can be worthwhile to harness machine learning for streamlining optimal MOFs. Furthermore, cost-efficiency is a key factor to consider during the design of a catalyst. While noble metal-based MOFs may exhibit high activity, their cost might eventually surpass their performance benefits. Therefore, using non-noble metals is highly desirable, especially from the perspective of economic viability.

### 5.3. Technological hurdles towards commercialization

Several companies in the world are leveraging the unique properties of MOFs to introduce as new porous materials into the market. However, in order to commercialize MOFs as electrocatalysts into the market, several challenges must be addressed. For commercialization, stability under redox conditions is one of the most critical metrics. In practical scenario, catalysts that degrade after only a few cycles cannot be considered cost-effective for long-term operation. For this reason, MOFs must possess high stability to be viable for commercial use. Furthermore, the heterogeneity of MOFs should be preserved. If metal ions leach during reactions, the method for collecting them needs to be considered, which incurs additional costs. Therefore, it is essential that even after conducting many cycles, remarkable metal ions should not be observed. The second thing is scalability. To expand the market

for MOFs, they need to be synthesized on a kilogram scale with adequate safety.

### 5.4. Improving MOFs' electrocatalytic activity for the NRR

The first requirement for enhancing the NRR catalytic performance of MOFs is to achieve a suitable level of hydrophobicity. This is due to the fact that the HER, which suppresses the NRR, becomes more favorable in a hydrophilic environment. Therefore, it is essential to manage the reaction conditions to minimize the occurrence of the HER. To establish an optimal hydrophobic state, one approach is to introduce hydrophobic functional groups into the MOF structure. Another essential factor for improving the NRR activity is the optimization of the active sites: purposely creating defect structures or utilizing multiple metals, as highlighted in previous discussion. In addition to these approaches, it is also believed that the use of multivariate MOFs can further enhance NRR catalytic activity. As demonstrated here, there are still some factors that can contribute to increasing the electrocatalytic activity of MOFs for the NRR. These suggestions possess the potential to guide the design of MOFs with higher catalytic activity in the future.

### 5.5. Standardization

As noted in this review, the activities of MOFs are evaluated at various voltages where the highest performance is obtained. However, without the standardization of such parameters, comparing the activities of these MOFs is inappropriate and a lack of uniformity in measurement conditions persists. Therefore, it is necessary to standardize some parameters such as the amount of catalyst, the kind and amount of electrolyte, counter electrode, voltage, the method of  $\text{NH}_3$  detection, *etc.*, which will lead to proper evaluation.

## 6. Concluding remarks

To sum up, MOFs have come to the fore as potential electrocatalysts for the NRR due to their structural tailorability and variety, extensive porosity and controllability over catalytically active sites. The pore space of MOFs can be harnessed to enhance reduction activity. Considerable research has been devoted to the enhancement of  $\text{N}_2$  adsorption capacity, introduction of redox-active sites, and boosting the reaction kinetics. Future research can be directed towards a deeper understanding of the mechanism, which in turn can lead towards the rational design of heterogeneous MOF catalysts.

## Author contributions

R. N.: information collection, writing original draft and editing; S. D.: conceptualization, supervision, review and editing; Y. N.: conceptualization, supervision, review and editing.

## Conflicts of interest

The authors declare no competing financial interest.



## Abbreviations

NiRu <sub>x</sub> -BDC	Ru-introduced Ni <sub>2</sub> (OH) <sub>2</sub> (C <sub>8</sub> H <sub>4</sub> O <sub>4</sub> );
BTC	Benzene-1,3,5-tricarboxylate;
NiCo-UMOFN	Ni and Co ultrathin MOF nanosheet;
CoBDC	Co <sub>2</sub> (OH) <sub>2</sub> (C <sub>8</sub> H <sub>4</sub> O <sub>4</sub> );
Fc	Carboxyferrocene;
Cu-BTC	Cu <sub>3</sub> (BTC) <sub>2</sub> (H <sub>2</sub> O) <sub>x</sub> ;
Cu-bipy-BTC	[Cu <sub>2</sub> (OH)(bipy) <sub>2</sub> (BTC) <sub>3</sub> ·2H <sub>2</sub> O] <sub>n</sub> ;
Bipy	2,2'-Bipyridine;
HITP	2,3,6,7,10,11-Hexamino-triphenylene;
BmimBF <sub>4</sub>	1-Butyl-3-methylimidazolium tetrafluoroborate;
BmimOTf	1-Butyl-3-methylimidazolium trifluoromethanesulfonate;
BmimPF <sub>6</sub>	1-Butyl-3-methylimidazolium hexafluorophosphate;
BmimClO <sub>4</sub>	1-Butyl-3-methylimidazolium perchlorate;
MvK	Mars-van Krevelen;
TMN	Transition metal nitrides;
EDTA	Ethylenediaminetetraacetic acid;
LiCF <sub>3</sub> SO <sub>3</sub>	Lithium trifluoromethanesulfonate;
RHE	Reversible hydrogen electrode;
NPG	Nanoporous gold;
SG	Sodium gluconate;
GA	Glucaric acid;
NiFe-MOF	Ni <sub>0.81</sub> Fe <sub>0.19</sub> ((C <sub>12</sub> H <sub>6</sub> O <sub>4</sub> )(H <sub>2</sub> O) <sub>4</sub> );
PtNS	Pt nanosphere;
HHTP	2,3,6,7,10,11-Hexahydroxytriphenylene;
OAm	Oleylamine;
CNT	Carbon nanotube;
AuNPs	Au nanoparticles;
Fe <sub>x</sub> Co <sub>y</sub> MOF-P <sub>2</sub> W <sub>18</sub>	[Fe <sub>x</sub> Co <sub>y</sub> (Pbpy) <sub>9</sub> (ox) <sub>6</sub> (H <sub>2</sub> O) <sub>6</sub> ][P <sub>2</sub> W <sub>18</sub> O <sub>62</sub> ]·3H <sub>2</sub> O;
UiO-S	UiO-66-SO <sub>3</sub> ;
PDMS	Polydimethylsiloxane;
Al-Fum MOF	Aluminum-fumarate MOF;
HPMo	Phosphomolybdic acid

## Acknowledgements

This study received financial support from the Scientific Research on Innovative Areas "Aquatic Functional Materials" (grant no. 22H04562), the Japan Society for the Promotion of Science (JSPS) KAKENHI (grant no. 20H02698, 22K19012, and 23H00289), the Yazaki Memorial Foundation for Science and Technology, and the Ogasawara Foundation for the Promotion of Science and Engineering.

## References

- O. M. Yaghi, G. Li and H. Li, *Nature*, 1995, **378**, 703–706.
- M. Kondo, T. Yoshitomi, H. Matsuzaka, S. Kitagawa and K. Seki, *Angew. Chem., Int. Ed. Engl.*, 1997, **36**, 1725–1727.
- H.-C. Zhou, J. R. Long and O. M. Yaghi, *Chem. Rev.*, 2012, **112**, 673–674.

- Z. Chen, K. O. Kirlikovali, P. Li and O. K. Farha, *Acc. Chem. Res.*, 2022, **55**, 579–591.
- H. Furukawa, K. E. Cordova, M. O'Keeffe and O. M. Yaghi, *Science*, 2013, **341**, 1230444.
- S. Kitagawa and R. Matsuda, *Coord. Chem. Rev.*, 2007, **251**, 2490–2509.
- S. Qiu, M. Xue and G. Zhu, *Chem. Soc. Rev.*, 2014, **43**, 6116–6140.
- R. C. Huxford, J. Della Rocca and W. Lin, *Curr. Opin. Chem. Biol.*, 2010, **14**, 262–268.
- W. Xu and O. M. Yaghi, *ACS Cent. Sci.*, 2020, **6**, 1348–1354.
- P. Horcajada, R. Gref, T. Baati, P. K. Allan, G. Maurin, P. Couvreur, G. Férey, R. E. Morris and C. Serre, *Chem. Rev.*, 2012, **112**, 1232–1268.
- L. E. Kreno, K. Leong, O. K. Farha, M. Allendorf, R. P. Van Duyne and J. T. Hupp, *Chem. Rev.*, 2012, **112**, 1105–1125.
- M. Kurmoo, *Chem. Soc. Rev.*, 2009, **38**, 1353–1379.
- D.-W. Lim and H. Kitagawa, *Chem. Rev.*, 2020, **120**, 8416–8467.
- S. Majumdar, S. M. Moosavi, K. M. Jablonka, D. Ongari and B. Smit, *ACS Appl. Mater. Interfaces*, 2021, **13**, 61004–61014.
- S. M. Rogers, C. R. A. Catlow, D. Gianolio, P. P. Wells and N. Dimitratos, *Faraday Discuss.*, 2018, **208**, 443–454.
- G.-G. Luo, Z.-H. Pan, B.-L. Han, G.-L. Dong, C.-L. Deng, M. Azam, Y.-W. Tao, J. He, C.-F. Sun and D. Sun, *Angew. Chem., Int. Ed.*, 2023, **62**, e202306849.
- Z. Chen, E. Vorobyeva, S. Mitchell, E. Fako, M. A. Ortuño, N. López, S. M. Collins, P. A. Midgley, S. Richard, G. Vilé and J. Pérez-Ramírez, *Nat. Nanotechnol.*, 2018, **13**, 702–707.
- Y. Zhao, K. R. Yang, Z. Wang, X. Yan, S. Cao, Y. Ye, Q. Dong, X. Zhang, J. E. Thorne, L. Jin, K. L. Materna, A. Trimpalis, H. Bai, S. C. Fakra, X. Zhong, P. Wang, X. Pan, J. Guo, M. Flytzani-Stephanopoulos, G. W. Brudvig, V. S. Batista and D. Wang, *Proc. Natl. Acad. Sci. U.S.A.*, 2018, **115**, 2902–2907.
- A. Corma, L. T. Nemeth, M. Renz and S. Valencia, *Nature*, 2001, **412**, 423–425.
- N. S. Ali, Z. T. Alismael, H. S. Majdi, H. G. Salih, M. A. Abdulrahman, N. M. Cata Saady and T. M. Albayati, *Heliyon*, 2022, **8**, e09737.
- R. Nakatani, S. Biswas, T. Irie, J. Sakai, D. Hirayama, T. Kawawaki, Y. Niihori, S. Das and Y. Negishi, *Nanoscale*, 2023, **15**, 16299–16306.
- Q. Fang, S. Gu, J. Zheng, Z. Zhuang, S. Qiu and Y. Yan, *Angew. Chem., Int. Ed.*, 2014, **53**, 2878–2882.
- A. Corma, *Faraday Discuss.*, 2016, **188**, 9–20.
- D. Bao, Q. Zhang, F.-L. Meng, H.-X. Zhong, M.-M. Shi, Y. Zhang, J.-M. Yan, Q. Jiang and X.-B. Zhang, *Adv. Mater.*, 2017, **29**, 1604799.
- J. Humphreys, R. Lan and S. Tao, *Adv. Energy Sustainability Res.*, 2021, **2**, 2000043.
- K. H. R. Rouwenhorst, A. G. J. Van der Ham and L. Lefferts, *Int. J. Hydrogen Energy*, 2021, **46**, 21566–21579.
- D. Liu, M. Chen, X. Du, H. Ai, K. H. Lo, S. Wang, S. Chen, G. Xing, X. Wang and H. Pan, *Adv. Funct. Mater.*, 2021, **31**, 2008983.





- 28 Y. Yao, H. Wang, X.-z. Yuan, H. Li and M. Shao, *ACS Energy Lett.*, 2019, **4**, 1336–1341.
- 29 X. Guo, H. Du, F. Qu and J. Li, *J. Mater. Chem. A*, 2019, **7**, 3531–3543.
- 30 Y. H. Moon, N. Y. Kim, S. M. Kim and Y. J. Jang, *Catalysts*, 2022, **12**, 1015.
- 31 K. Liu, P. Cao, W. Chen, C. I. Ezech, Z. Chen, Y. Luo, Q. Liu, H. Zhao, Z. Rui, S. Gao, Z. Yin, X. Sun and X. Yu, *Mater. Adv.*, 2022, **3**, 1359–1400.
- 32 R. Akter, S. S. Shah, M. A. Ehsan, M. N. Shaikh, M. H. Zahir, M. A. Aziz and A. J. S. Ahammad, *Chem.–Asian J.*, 2024, **19**, e202300797.
- 33 X. Wen and J. Guan, *Nanoscale*, 2020, **12**, 8065–8094.
- 34 W. Xiong, H. Yin, T. Wu and H. Li, *Chem.–Eur. J.*, 2023, **29**, e202202872.
- 35 Q. Zhang and J. Guan, *Adv. Funct. Mater.*, 2020, **30**, 2000768.
- 36 W. Zhang, J. Low, R. Long and Y. Xiong, *EnergyChem*, 2020, **2**, 100040.
- 37 Y. Peng, S. Sanati, A. Morsali and H. García, *Angew. Chem., Int. Ed.*, 2023, **62**, e202214707.
- 38 L. Sun, M. G. Campbell and M. Dincă, *Angew. Chem., Int. Ed.*, 2016, **55**, 3566–3579.
- 39 S. K. Bhardwaj, N. Bhardwaj, R. Kaur, J. Mehta, A. L. Sharma, K.-H. Kim and A. Deep, *J. Mater. Chem. A*, 2018, **6**, 14992–15009.
- 40 H. He, H.-M. Wen, H.-K. Li and H.-W. Zhang, *Coord. Chem. Rev.*, 2022, **471**, 214761.
- 41 Y. Zhu, H. Ji, T. Huang, Y. Sun and H. Pang, *Adv. Sustainable Syst.*, 2024, 2400225.
- 42 Z. Zhu, J. Duan and S. Chen, *Small*, 2024, **20**, 2309119.
- 43 I. E. Khalil, C. Xue, W. Liu, X. Li, Y. Shen, S. Li, W. Zhang and F. Huo, *Adv. Funct. Mater.*, 2021, **31**, 2010052.
- 44 X. Han, S. Yang and M. Schröder, *J. Am. Chem. Soc.*, 2023, **145**, 1998–2012.
- 45 Y. Yu, Y. Li, Y. Fang, L. Wen, B. Tu and Y. Huang, *Appl. Catal., B*, 2024, **340**, 123161.
- 46 L. Tang, Q. Xu, Y. Zhang, W. Chen and M. Wu, *Electrochem. Energy Rev.*, 2022, **5**, 32–81.
- 47 B. Nohra, H. El Moll, L. M. Rodriguez Albelo, P. Mialane, J. Marrot, C. Mellot-Draznieks, M. O'Keeffe, R. Ngo Biboum, J. Lemaire, B. Keita, L. Nadjjo and A. Dolbecq, *J. Am. Chem. Soc.*, 2011, **133**, 13363–13374.
- 48 W. R. McNamara, Z. Han, P. J. Alperin, W. W. Brennessel, P. L. Holland and R. Eisenberg, *J. Am. Chem. Soc.*, 2011, **133**, 15368–15371.
- 49 A. J. Clough, J. W. Yoo, M. H. Mecklenburg and S. C. Marinescu, *J. Am. Chem. Soc.*, 2015, **137**, 118–121.
- 50 Y. Sun, Z. Xue, Q. Liu, Y. Jia, Y. Li, K. Liu, Y. Lin, M. Liu, G. Li and C.-Y. Su, *Nat. Commun.*, 2021, **12**, 1369.
- 51 K. F. Babu, M. A. Kulandainathan, I. Katsounaros, L. Rassaei, A. D. Burrows, P. R. Raithby and F. Marken, *Electrochem. Commun.*, 2010, **12**, 632–635.
- 52 S. Zhao, Y. Wang, J. Dong, C.-T. He, H. Yin, P. An, K. Zhao, X. Zhang, C. Gao, L. Zhang, J. Lv, J. Wang, J. Zhang, A. M. Khattak, N. A. Khan, Z. Wei, J. Zhang, S. Liu, H. Zhao and Z. Tang, *Nat. Energy*, 2016, **1**, 16184.
- 53 Z. Xue, K. Liu, Q. Liu, Y. Li, M. Li, C.-Y. Su, N. Ogiwara, H. Kobayashi, H. Kitagawa, M. Liu and G. Li, *Nat. Commun.*, 2019, **10**, 5048.
- 54 J. Mao, L. Yang, P. Yu, X. Wei and L. Mao, *Electrochem. Commun.*, 2012, **19**, 29–31.
- 55 E. M. Miner, T. Fukushima, D. Sheberla, L. Sun, Y. Surendranath and M. Dincă, *Nat. Commun.*, 2016, **7**, 10942.
- 56 Z. Liang, H. Guo, G. Zhou, K. Guo, B. Wang, H. Lei, W. Zhang, H. Zheng, U.-P. Apfel and R. Cao, *Angew. Chem., Int. Ed.*, 2021, **60**, 8472–8476.
- 57 R. Hinogami, S. Yotsuhashi, M. Deguchi, Y. Zenitani, H. Hashiba and Y. Yamada, *ECS Electrochem. Lett.*, 2012, **1**, H17.
- 58 X. Kang, Q. Zhu, X. Sun, J. Hu, J. Zhang, Z. Liu and B. Han, *Chem. Sci.*, 2016, **7**, 266–273.
- 59 Y.-L. Qiu, H.-X. Zhong, T.-T. Zhang, W.-B. Xu, P.-P. Su, X.-F. Li and H.-M. Zhang, *ACS Appl. Mater. Interfaces*, 2018, **10**, 2480–2489.
- 60 L. Yang, S. Kinoshita, T. Yamada, S. Kanda, H. Kitagawa, M. Tokunaga, T. Ishimoto, T. Ogura, R. Nagumo, A. Miyamoto and M. Koyama, *Angew. Chem., Int. Ed.*, 2010, **49**, 5348–5351.
- 61 H. Gu, W. Chen and X. Li, *J. Mater. Chem. A*, 2022, **10**, 22331–22353.
- 62 S. Y. Park, Y. J. Jang and D. H. Youn, *Catalysts*, 2023, **13**, 639.
- 63 W. T. Bolleter, C. J. Bushman and P. W. Tidwell, *Anal. Chem.*, 1961, **33**, 592–594.
- 64 C. J. Patton and S. Crouch, *Anal. Chem.*, 1977, **49**, 464–469.
- 65 D. Scheiner, *Water Res.*, 1976, **10**, 31–36.
- 66 T. Tsuboi, Y. Hirano, Y. Shibata and S. Motomizu, *Anal. Sci.*, 2002, **18**, 1141–1144.
- 67 M. Nichols and C. Willits, *J. Am. Chem. Soc.*, 1934, **56**, 769–774.
- 68 A. Vanselow, *Ind. Eng. Chem., Anal. Ed.*, 1940, **12**, 516–517.
- 69 H. Jeong, J. Park and H. Kim, *J. Chem.*, 2013, **2013**, 359217.
- 70 F. C. Koch and T. L. McMeekin, *J. Am. Chem. Soc.*, 1924, **46**, 2066–2069.
- 71 Y. Fu, K. Li, M. Batmunkh, H. Yu, S. Donne, B. Jia and T. Ma, *ACS Appl. Mater. Interfaces*, 2020, **12**, 44830–44839.
- 72 S. Chen, S. Perathoner, C. Ampelli, C. Mebrahtu, D. Su and G. Centi, *Angew. Chem., Int. Ed.*, 2017, **56**, 2699–2703.
- 73 G. W. Watt and J. D. Chrisp, *Anal. Chem.*, 1952, **24**, 2006–2008.
- 74 X. Zhao, F. Yin, N. Liu, G. Li, T. Fan and B. Chen, *J. Mater. Sci.*, 2017, **52**, 10175–10185.
- 75 L. Zhao, X. Kuang, C. Chen, X. Sun, Z. Wang and Q. Wei, *Chem. Commun.*, 2019, **55**, 10170–10173.
- 76 X. Yi, X. He, F. Yin, T. Yang, B. Chen and G. Li, *J. Mater. Sci.*, 2020, **55**, 12041–12052.
- 77 W. Xiong, X. Cheng, T. Wang, Y. Luo, J. Feng, S. Lu, A. M. Asiri, W. Li, Z. Jiang and X. Sun, *Nano Res.*, 2020, **13**, 1008–1012.
- 78 Y. Cao, P. Li, T. Wu, M. Liu and Y. Zhang, *Chem.–Asian J.*, 2020, **15**, 1272–1276.
- 79 P. Liu, P. Jing, X. Xu, B. Liu and J. Zhang, *ACS Appl. Energy Mater.*, 2021, **4**, 12128–12136.



- 80 Y. Sun, B. Xia, S. Ding, L. Yu, S. Chen and J. Duan, *J. Mater. Chem. A*, 2021, **9**, 20040–20047.
- 81 X. He, F. Yin, X. Yi, T. Yang, B. Chen, X. Wu, S. Guo, G. Li and Z. Li, *ACS Appl. Mater. Interfaces*, 2022, **14**, 26571–26586.
- 82 L. Shi, P. Guo, F. Yin, A. A. M. Ahmed Al-Anzah, Z. Ni, J. Zhang, G. Li and B. Chen, *Catal. Today*, 2024, **433**, 114662.
- 83 B. Han, L. Zhong, C. Chen, J. Ding, C. Lee, J. Liu, M. Chen, S. Tso, Y. Hu, C. Lv, Y. Han, B. Liu and Q. Yan, *Small*, 2024, **20**, 2307506.
- 84 Y. Sun, W. Fan, Y. Li, N. L. D. Sui, Z. Zhu, Y. Zhou and J.-M. Lee, *Adv. Mater.*, 2024, **36**, 2306687.
- 85 W. Li, W. Fang, C. Wu, K. N. Dinh, H. Ren, L. Zhao, C. Liu and Q. Yan, *J. Mater. Chem. A*, 2020, **8**, 3658–3666.
- 86 J. Duan, Y. Sun, S. Chen, X. Chen and C. Zhao, *J. Mater. Chem. A*, 2020, **8**, 18810–18815.
- 87 J. Tan, X. He, F. Yin, X. Liang and G. Li, *Int. J. Hydrogen Energy*, 2021, **46**, 31647–31658.
- 88 M. Yang, X. Wang, C. J. Gómez-García, Z. Jin, J. Xin, X. Cao, H. Ma, H. Pang, L. Tan, G. Yang and Y. Kan, *Adv. Funct. Mater.*, 2023, **33**, 2214495.
- 89 S. Li, K. Cheng, L. Ma, L. Zhang, F. Li and Q. Cheng, *Inorg. Chem.*, 2024, **63**, 8366–8375.
- 90 M. Cong, X. Chen, K. Xia, X. Ding, L. Zhang, Y. Jin, Y. Gao and L. Zhang, *J. Mater. Chem. A*, 2021, **9**, 4673–4678.
- 91 M. Romero-Angel, R. Amrine, B. Ávila-Bolívar, N. Almora-Barrios, C. R. Ganivet, N. M. Padial, V. Montiel, J. Solla-Gullón, S. Tatay and C. Martí-Gastaldo, *J. Mater. Chem. A*, 2024, **12**, 10956–10964.
- 92 H. K. Lee, C. S. L. Koh, Y. H. Lee, C. Liu, I. Y. Phang, X. Han, C.-K. Tsung and X. Y. Ling, *Sci. Adv.*, 2018, **4**, eaar3208.
- 93 C. S. L. Koh, H. K. Lee, H. Y. Fan Sim, X. Han, G. C. Phan-Quang and X. Y. Ling, *Chem. Mater.*, 2020, **32**, 1674–1683.
- 94 H. He, Q.-Q. Zhu, Y. Yan, H.-W. Zhang, Z.-Y. Han, H. Sun, J. Chen, C.-P. Li, Z. Zhang and M. Du, *Appl. Catal., B*, 2022, **302**, 120840.
- 95 L. Wen, K. Sun, X. Liu, W. Yang, L. Li and H.-L. Jiang, *Adv. Mater.*, 2023, **35**, 2210669.
- 96 Y. Yang, S.-Q. Wang, H. Wen, T. Ye, J. Chen, C.-P. Li and M. Du, *Angew. Chem., Int. Ed.*, 2019, **58**, 15362–15366.
- 97 Z. Ni, F. Yin, J. Zhang, G. Kofie, G. Li, B. Chen, P. Guo and L. Shi, *Chem.–Eur. J.*, 2024, **30**, e202401010.
- 98 H. Y. F. Sim, J. R. T. Chen, C. S. L. Koh, H. K. Lee, X. Han, G. C. Phan-Quang, J. Y. Pang, C. L. Lay, S. Pedireddy, I. Y. Phang, E. K. L. Yeow and X. Y. Ling, *Angew. Chem., Int. Ed.*, 2020, **59**, 16997–17003.
- 99 Y. Lv, Y. Wang, M. Yang, Z. Mu, S. Liu, W. Ding and M. Ding, *J. Mater. Chem. A*, 2021, **9**, 1480–1486.
- 100 S. Chen, F. Yin, X. He and J. Tan, *ChemistrySelect*, 2023, **8**, e202204988.
- 101 X. Liang, X. Ren, Q. Yang, L. Gao, M. Gao, Y. Yang, H. Zhu, G. Li, T. Ma and A. Liu, *Nanoscale*, 2021, **13**, 2843–2848.
- 102 J. Duan, D. Shao, X. He, Y. Lu and W. Wang, *Colloids Surf., A*, 2021, **619**, 126529.
- 103 W.-Y. Xu, C. Li, F.-L. Li, J.-Y. Xue, W. Zhang, H. Gu, B. F. Abrahams and J.-P. Lang, *Sci. China: Chem.*, 2022, **65**, 885–891.
- 104 Y. Liu, X. Meng, Z. Zhao, K. Li and Y. Lin, *Nanomaterials*, 2022, **12**, 2964.
- 105 S. Mukherjee, D. A. Cullen, S. Karakalos, K. Liu, H. Zhang, S. Zhao, H. Xu, K. L. More, G. Wang and G. Wu, *Nano Energy*, 2018, **48**, 217–226.
- 106 P. Song, L. Kang, H. Wang, R. Guo and R. Wan, *ACS Appl. Mater. Interfaces*, 2019, **11**, 12408–12414.
- 107 P. Wang, S. Zhao, Y. Xing, Z. Liu, Y. Xu, S. Li, S. Wang and J. Li, *Microporous Mesoporous Mater.*, 2024, **368**, 113031.
- 108 Z. Geng, Y. Liu, X. Kong, P. Li, K. Li, Z. Liu, J. Du, M. Shu, R. Si and J. Zeng, *Adv. Mater.*, 2018, **30**, 1803498.
- 109 F. Lü, S. Zhao, R. Guo, J. He, X. Peng, H. Bao, J. Fu, L. Han, G. Qi, J. Luo, X. Tang and X. Liu, *Nano Energy*, 2019, **61**, 420–427.
- 110 F. Wang, L. Zhang, T. Wang, F. Zhang, Q. Liu, H. Zhao, B. Zheng, J. Du and X. Sun, *Inorg. Chem.*, 2021, **60**, 7584–7589.

